A VALIDATION STUDY OF CLOUD SCENE
SIMULATION MODEL TEMPORAL
PERFORMANCE

THESIS

D. Glenn Kerr, Captain, USAF
AFIT/GM/ENP/99M-08

19990402 025

DEPARTMENT OF THE AIR FORCE
AIR UNIVERSITY
AIR FORCE INSTITUTE OF TECHNOLOGY

Wright-Patterson Air Force Base, Ohio

A VALIDATION STUDY OF CLOUD SCENE

SIMULATION MODEL TEMPORAL PERFORMANCE

THESIS

D. Glenn Kerr, Captain, USAF

AFIT/GM/ENP/99M-08

The views expressed in this thesis are those of the author, and do not reflect the

official policy or position of the Department of Defense, or the U.S. Government.

AFIT/GM/ENP/99M-08

A VALIDATION STUDY OF CLOUD SCENE

SIMULATION MODEL TEMPORAL PERFORMANCE

THESIS

Presented to the Faculty of the Graduate School of Engineering

of the Air Force Institute of Technology Air University

Air Education and Training Command In Partial Fulfillment of the Requirements

for the

Degree of Master of Science in Meteorology

D. Glenn Kerr, B.A.

Captain, USAF

January 1999

A VALIDATION STUDY OF CLOUD SCENE

SIMULATION MODEL TEMPORAL PERFORMANCE

D. Glenn Kerr, B.A.

Captain, USAF

Approved:

_____   _____
Michael K. Walters, Lt Col, USAF   3 MAR 99
Chairman, Advisory Committee   Date
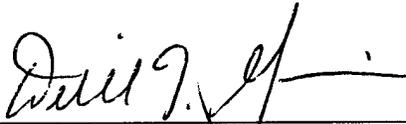
_____   _____
Derrill T. Goldizen, Maj, USAF   4 Mar 99
Member, Advisory Committee   Date
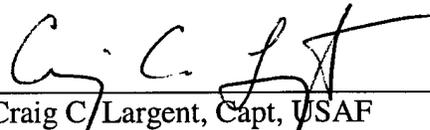
_____   _____
Craig C. Largent, Capt, USAF   5 Mar 99
Member, Advisory Committee   Date

Acknowledgements

Let me begin by thanking Lieutenant Colonel John R. Lanicci for pushing me in the direction that led to this project. I would like to thank my thesis advisor, Lieutenant Colonel Michael K. Walters, for his interest in the project. His assistance helped me to narrow my focus and work through the difficulties that arose. I would also like to thank the other members of my committee, Major Derrill Goldizen, and Captain Craig Largent for their valuable input during research, and their help with completing this document. I must also thank Master Sergeant Pete Rahe for his work to ensure I always had sufficient disk space for the enormous amounts of data produced during the course of this research, and Dave Doak, for providing a Silicon Graphics computer to the Weather Lab to run the cloud models.

Further afield, I would like to thank the folks at Phillips Laboratory, Hanscom AFB, Massachusetts, for their exceptional assistance and patience during the course of this project. Specifically, I thank Joel B. Mozer, who provided the idea for this project. His advice and comments during many conversations proved invaluable. Also, my thanks go Steve Ayer and Guy Seeley, whose computer expertise was greatly appreciated. Finally, thanks go to Tim Hiett for providing the data set used for the project, and for his help with accessing and processing the data.

I would like to thank my wife, Nichole, for her support and encouragement during this time. Her prodigious knowledge about word processing software and her editing skills were greatly needed and appreciated. I would also like to thank my wonderful children: Stephanie, Jon, Seth, Ben, Ian, and Evan. Their support has been critical as I have been attending college most of their lives. Let me also thank my Mom and Dad for their encouragement and unconditional support for all my efforts. Finally, I must thank God for providing me the insight and strength I've needed .

Table Of Contents

LIST OF FIGURES

LIST OF TABLES

AFIT/GM/ENP/99M-08

ABSTRACT

Cloud Scene Simulation Model (CSSM) temporal performance was validated by comparing the cloud forcing signatures on observed radiometric time series with those derived from CSSM output for initial conditions similar to that for the observed data. Observed radiometric data was collected by a normal incidence pyraheliometer sensitive to wavelengths in the range .3μm to 3μm. Simulation radiometric time series data was derived by applying the following process to each case study. CSSM cloud liquid water content (CLWC) grids were converted to grids of slant path optical depth values by the Fast Map post processor to the CSSM. A ray tracing routine then integrated the slant path optical depth values along a path from the position of the sun through each cloud volume to a point at its base. The position of the sun was fixed by ephemeris calculations for the time and location of the case study. The integrated optical depth values were then used with a modified form of Beer's Law to derive radiometric time series values.

Subjective and statistical comparison of the observed and corresponding simulation time series data were then made. The statistical comparison used correlograms, variograms and power law analyses to determine whether CSSM cloud field evolution with time proceeded in a realistic manner.

Results indicate that CSSM cloud fields do not evolve in a realistic manner. Radiometric traces derived from simulation data lack small scale variations present in the observed data, while large scale variations in the simulation data are exaggerated.

A VALIDATION STUDY OF CLOUD SCENE SIMULATION MODEL TEMPORAL PERFORMANCE

1. *Introduction*

The role of modeling and simulation has been steadily increasing as budgetary constraints have forced the military to seek more efficient and cost effective means to accomplish training and development of technology and defense applications. Advances in computers and networking technology now make complex models and realistic simulations possible. Accurate, high fidelity atmospheric descriptions are required to achieve the realism necessary for effective operation of sophisticated applications, such as immersive flight simulators, or large-scale distributive interactive environments. The Cloud Scene Simulation Model (CSSM) has proven to be a valuable tool in this pursuit (Cianciolo and Rasmussen 1992).

1.1 *Background*

Originally developed by the U. S. Air Force Phillips Laboratory and The Analytical Sciences Corporation (TASC), Inc. for the Smart Weapons Operability Enhancement (SWOE) program, the CSSM was designed to simulate realistic cloud fields for use in radiometric sensor evaluation studies. The model supports multi-layer cloud generation for all major cloud types consistent with large-scale input weather conditions. This user-specified input includes cloud type, fractional sky coverage, mean cloud base and maximum cloud top for each layer modeled, as well as atmospheric

information such as temperature, moisture and mean wind speed and direction (Cianciolo and Rasmussen 1992).

The current version of the CSSM is based on the older version, but has been greatly modified and enhanced to characterize the weather environment for Department of Defense (DoD) simulation and training applications (Hembree 1997). The model now supports larger scale simulations in both space and time. A precipitation model is included, and a wider variety of cloud types can now be modeled, including structured clouds such as cloud streets and wave clouds. In addition to input of general meteorological conditions, the model can accept gridded observational data, or a combination of the two types of input (Cianciolo and Rasmussen 1992). Interface utilities have been developed to allow output from the Fifth Generation Mesoscale Model (MM5) to be used as gridded input to the CSSM, effectively enabling simulations to reflect model forecast weather conditions (Setayesh 1996).

It is important to realize that the CSSM was not designed to precisely model the physical processes within clouds. Such models are extremely expensive, in a computational sense, and are unable to generate cloud fields over a large domain at the minimum rate necessary to support real time simulation and training applications. Instead, the CSSM is an empirical model that uses stochastic methods to generate multi-layer cloud water and precipitable water fields. To produce these fields, the model makes use of a core fractal algorithm known as the rescale and add (RSA) algorithm (Saupe 1989). Parameters governing the character of the cloud fields generated by the RSA algorithm have been tuned to ensure that the cloud fields generated by the CSSM are

statistically representative of the weather-state for the input conditions (Cianciolo and Rasmussen 1992; Cianciolo and Raffensberger 1996a; Turkington et al. 1998).

1.2   Statement of the Problem

The RSA algorithm operates in four dimensions, three spatial and one temporal, as will be discussed in more detail in chapter 2. Parameter values used in the RSA algorithm were selected by analyzing measurements of cloud liquid water content (CLWC) taken by aircraft as they flew transects through different types of clouds. Simulated cloud fields were then produced with the CSSM for similar meteorological conditions and compared to the real data. The RSA parameters were then adjusted using an iterative process, so that the statistical characteristics of CLWC paths through simulated clouds matched those of the actual clouds (Cianciolo and Raffensberger 1996a; Turkingtion et al. 1998). This approach was effective for tuning the RSA algorithm to simulate the three-dimensional, spatial characteristics of various clouds, however it was unable to capture the variation of these clouds over time.

During model development, temporal RSA parameters were selected subjectively to yield realistic-looking cloud evolution, that is, growth and dissipation of individual elements over short time periods (Cianciolo and Rasmussen 1992). How well does the CSSM handle the evolution of cloud elements through time using these subjective parameters? Is there an effective method to infer the spatial variation of cloud features over time-periods on the order of an hour? If so, then it is reasonable to expect that the temporal behavior of the CSSM can be objectively judged.

3

1.2.1 Objectives

The goal of this thesis was to evaluate the temporal performance of the CSSM. This involved producing time series data of cloud forcing signatures on radiometric signals based on cloud fields generated by the CSSM for given initial meteorological and cloud conditions. These were then compared with actual cloud forcing signatures on radiometric time series data for those conditions used to initialize the CSSM. The real and simulated time series were then objectively compared using time series analysis techniques in both the time and frequency domains to estimate the accuracy of model performance over time.

1.2.2 Scope

This study addresses temporal evolution of stratiform cloud types over time-periods on the order of one hour. Sky conditions for the cases comprising the study were nearly completely overcast to ensure continuous cloud forcing of the radiometric signal at the surface. The CSSM output domain was a cubical grid ten kilometers on a side, with a resolution of 100 meters. Its size was determined by the height of the real clouds being simulated.

1.2.3 Benefit of Solving the Problem

Until now, only the spatial structure of cloud fields generated by the CSSM has been verified to be consistent with actual cloud fields under the same general meteorological conditions (Cianciolo and Raffensberger 1996a). The internal distribution of liquid water content within the simulated cloud fields has been validated, as mentioned

4

previously. In addition, the external macro-structure of these synthetic clouds has been

optimized to closely match radiometric imagery of real clouds (Turkingtion et al. 1998).

However, the behavior of the CSSM over time has never been objectively addressed and

is strongly suspected to be inaccurate (J. B. Mozer 1998, personal communication).

Validation of the CSSM's temporal performance will objectively determine whether it

produces cloud fields which vary with time in a realistic manner. This validation will

also serve as a benchmark for future temporal parameter tuning efforts, which could then

improve the overall realism of the many simulations of which the CSSM is already a part.

1.3   Procedure

The model validation was accomplished by comparing time series radiance

measurements collected under stratus cloud layers on overcast days with simulated time

series radiance measurements produced with synthetic cloud layers. Radiance

measurements were collected by a solar-tracking normal incidence pyraheliometer

sensitive to radiation from .3µm to 3µm. Radiometric time series data exhibit variations

in solar insolation due to clouds evolving as they advect over a heliometer. Since these

clouds are being advected as they evolve, an analysis of these data includes effects of

both spatial and temporal evolution. These measurements reflect the structure of the

cloud field as a reduction in measured radiance at the heliometer for optically thick

clouds passing between the instrument and the sun. It has been demonstrated that such

radiometric measurements provide an effective means of investigating the spatial

structure of a cloud field for broken clouds moving at relatively constant speed (Seeley et

al. 1997). This thesis uses this method to analyze the evolution of the structure of cloud

fields as they evolve through time, and then compares this evolution with that for simulated cloud fields. A complete description of the processes used in this study is given in Chapter 3. The following subsections briefly outline steps taken to conduct the study.

1.3.1 Model Initialization

Six case studies were selected from data collected on 11 and 12 July 1995, at Hanscom AFB, Massachusetts during the Air Combat Targeting/Electro-Optical Simulation (ACT/EOS) validation experiments. Each case study featured broken to overcast sky conditions containing stratiform cloud types, and was between 35 and 60 minutes in length. Radiometric time series observed at the test site for each case study were extracted from the ACT/EOS data set for comparison with simulation time series derived from CSSM output. Meteorological conditions observed at the test site during the times of each study were used to initialize the CSSM, and ten simulations were run for each case study using different random seed numbers as input to initialize the fractal field generation algorithm

1.3.2 Simulation Data Production and Processing

Once the CSSM has produced simulated cloud field time series for each study, the Fast Map postprocessor, described in section 2.4, then generates gridded volumes of slant path optical depth values corresponding to each CSSM cloud volume. Each volume represented the simulation domain at a particular minute of the time series.

A ray tracing routine was then used for each of these volumes to integrate slant

path optical depth values at each grid point along a path through simulation domain connecting a virtual pyraheliometer and the sun. Ephemeris calculations fixed the position of the sun for the time of each study and the location of the test site. This position was updated every minute to correspond to each output file in the time series, allowing the sun's trek through the sky with time to be faithfully simulated. Output from the ray tracing routine consisted of a time series of slant path optical depth values representing the changing optical depth of a simulated cloud field as it evolved with time.

Finally, the time series of optical depth values were used to create a simulated radiometric time series. A modified form of Beer's Law used the slant path optical depth values to derive radiance quantities for comparison with the observed data. Development of the modified Beer's Law equation is detailed in Appendix B. Use of this formula facilitated proper scaling of the simulated radiance values to the dynamic range of the observed data while preserving the temporal structure of the simulated time series, which was the focus of the study.

1.3.3 Data Analysis and Comparison

Once produced, the simulation radiometric data sets were analyzed and compared to the corresponding observed data. The first step in this process was to compare the radiometric traces in a qualitative manner to ensure that both simulation and observed time series exhibited the same characteristic features. These features include the amplitude and frequency of variations in the signal. Histograms of radiance values were also produced and compared qualitatively to determine whether the simulation data distributions were similar to that for the observed data in each case.

More objective statistical methods were also employed. Autocorrelation coefficients were calculated for each time series step and correlograms were produced. The first zero-crossing of the autocorrelation coefficients was determined to infer a characteristic correlation time scale for each data set, which could then be compared to the observed data. Variograms were also produced for each case. These allowed the differing degrees of small scale variability to be graphically compared.

Finally, power law analyses were accomplished for each series. These analyses sought to characterize the variability in each time series according to the slope of a least squares linear fit to a logarithmic plot of frequency versus power for each radiometric trace. A comparison of the slopes of these fit lines suggested whether small and large scale variations in the radiometric signal were similar or not.

1.4   Thesis Organization

Chapter 2 presents a synopsis of information found in the literature which contributes to the understanding of the problem. The term fractal is defined, and its application to the description of cloud fields in both space and time are discussed. The RSA model, CSSM, and Fast Map post-processor will be briefly described.

Chapter 3 describes the methodology used to evaluate CSSM performance. Processing of both real and simulation data will be outlined. A brief discussion of the radiative transfer theory used to produce the time series data will be given.

Chapter 4 discusses the statistical methods used to analyze and compare the time series data. Here, the results of the study will be summarized.

Finally, chapter 5 presents conclusions drawn from the data analysis.

Recommendations for future research will also be given.

2.   *Literature Review*

This chapter provides a survey of information found in the literature, which provides a background for understanding this work. It is useful to begin by defining the term *fractal*, since the cloud fields generated by this model are, essentially, fractals. Next, works are presented which justify the description of cloud characteristics as fractals in space and time. Following this, the re-scale and add (RSA) fractal-generating algorithm, which is central to the Cloud Scene Simulation Models (CSSM's) operation, is described. Then the CSSM is described in detail, as well as the Fast Map post processor. Finally, a previous study of cloud forcing on radiometric signatures is discussed.

2.1   Fractals

Fractals are shapes, which have structure at all scales, with no characteristic length (Mandelbrot 1983). In order to provide a clearer understanding of exactly what a fractal is, a discussion of how the concept of the fractal arose, and an illustration of how one may construct a fractal is offered.

Objects can be described by Euclidean geometry as having an integral number of dimensions. A line has one dimension, length; a square has two dimensions, length and height; and a cube adds the third dimension, depth. With these three dimensions, many shapes, which are essentially sets of related points in space, can be classified and studied. There are many sets of related points, shapes, which cannot be effectively described by Euclidean geometry. Examples include the shape of coastlines, trees, and clouds. In order to characterize and study these various shapes, dimensionality was redefined in

such a way that objects which could be described by Euclidean geometry retained their traditional dimension values. A line still had only one dimension, a square had two dimensions, and a cube had three. However, the other shapes could also be assigned dimensional values. The shapes in this latter class turned out to have fractional values of dimension. Benoit Mandelbrot coined the term *fractals* for such shapes (Mandelbrot 1983).

The fractal dimension of a set of points can be defined in various ways. These definitions sometimes result in different fractal dimensional values, so it is important to know how the dimension has been defined. One method, based on the widely used Hausdorff-Besicovitch dimension, is that of capacity (Lorenz 1996). This definition can be illustrated by considering a set of points in a plane which are bounded by a square. The square can be divided into four smaller squares, each one quarter of the original in size. Each of these squares can be divided into four pieces and each piece into four pieces. For a set of points covering the entire square, the number of squares used to cover the set of points increase by a factor of four for each division of the original square. For a line, the number of squares would eventually double at each step; and for a point, the number of squares would not grow. Thus, the number of squares increases as 2^2, 2^1 and 2^0 for each case, respectively. By successively noting the number of squares required to cover the set of points at each step, a dimension d can be defined according to $2^{n*d}=n$. Here n is the factor by which the number of squares needed to cover the set of points increases at each step.

In order to construct a fractal, define a set of points for which the number of squares needed to cover the set of points increases by 2^{n*d} for each step n, where d is not

11

an integer value. This can be accomplished, for example, by considering a set of points covering the entire square. Now divide this set into four equal squares and eliminate the points in the upper right quadrant. Doing this repeatedly an arbitrary number of times gives a shape as seen in Figure 2-1.
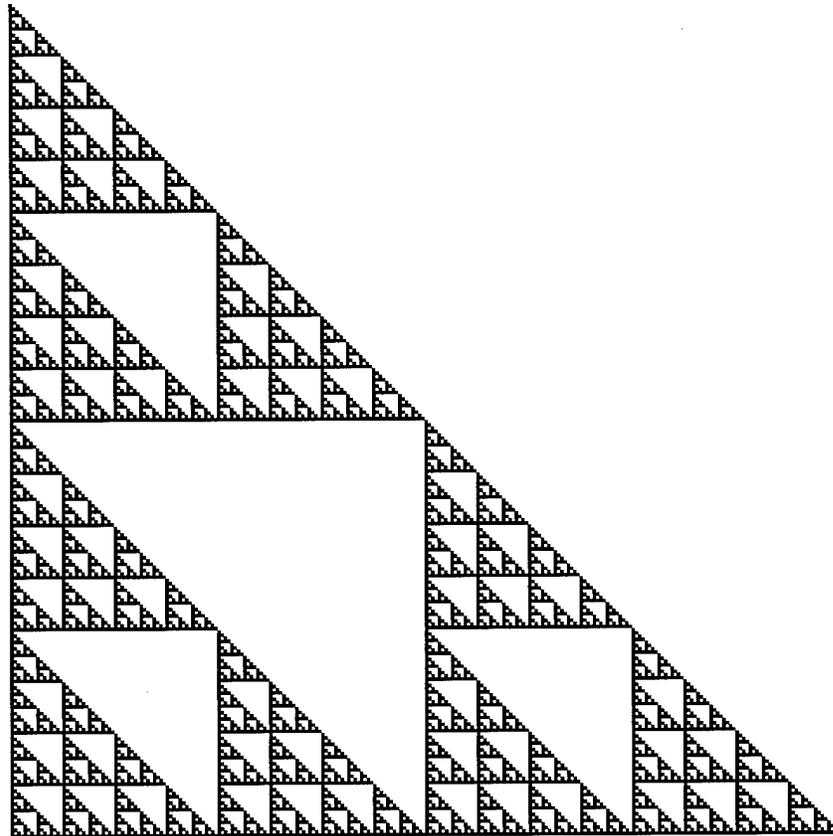
Figure 2-1. A triangular fractal with dimension, $d=1.586$.

Using a numerical bisection technique, it can be determined that the number of squares required to cover this set of points at each step increases by a factor of three (Burden and Faires, 1997). This gives $2^{n*d}=3$, or $d=1.586$, as shown in Table 2-1. Thus, a shape with fractional dimension, a *fractal*, has been created.

Table 2-1. Increase in the number of squares needed to cover a fractal with the Hausdorff-Besicovitch dimension $d=1.586$.

Step n	Function $f(n)=2n*d$	Number of Squares
1	$f(1)=21*1.586$	3
2	$f(2)=22*1.586$	9
3	$f(3)=23*1.586$	27
4	$f(4)=24*1.586$	81
5	$f(5)=25*1.586$	243

Notice the self-similarity of the features in Figure 2-1, as we observe increasingly smaller detail. This trait is commonly observed with fractals. Here, it is obvious because of the way the shape was defined. If we were to define the shape differently, by eliminating a random square at each step for instance, we would obtain a fractal with the same dimension. However, its appearance would be dramatically different as seen in Figure 2-2. Here the self-similarity is not as visually evident, but it does still exist in a statistical sense. It is this type of statistical self-similarity that is exhibit by clouds (Lorenz 1996).
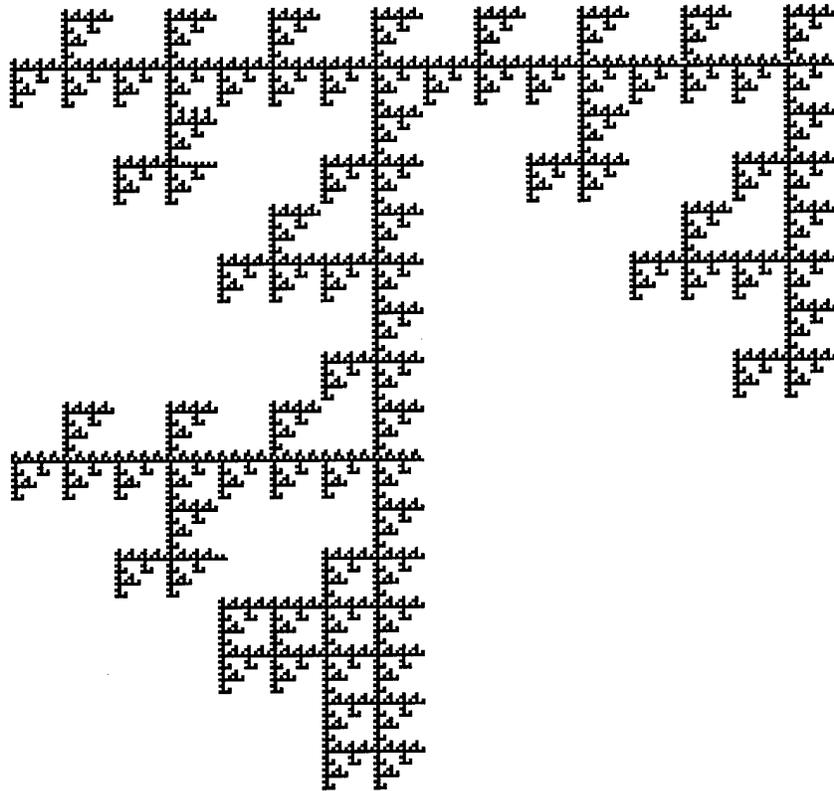
Figure 2-2. A random fractal with dimension, d=1.586.

2.1.1 Clouds as Fractals in Space

Often, to reduce the complexity of meteorological problems, clouds are modeled as lattices of disks, or collections of small cubes. In reality, clouds and cloud fields are observed to be irregular in shape and distribution at all scales. Consider a large cloud. It consists of bulges and lumps, which have smaller bulges and lumps on them. In fact, given an image containing only a cloud, it is difficult to determine the size of the image, without a point of reference for comparison. An essential feature of fractals is that they look the same at all scales. This characteristic leads to the effective description of clouds as fractal sets of points in space. The concept of the scaling fractal is a useful tool in this pursuit (Cahalen and Joseph 1989; Feder 1988).

14

The area – perimeter relationship is a common way to study fractals. It has been used to analyze the geometric structure of clouds in the horizontal plane (Lovejoy 1982). Infrared satellite images of optically thick clouds in the Indian Ocean, as well as digitized radar images of tropical rain areas were observed by Lovejoy to be related by:

$$P = C \cdot \sqrt[D]{A}. \qquad (2\text{-}1)$$

Here, C is a proportionality constant used to account for the resolution difference between satellite and radar data, and D is the fractal dimension. This relation was observed to hold for horizontal length scales between 1 and 1000 kilometers, with a fractal dimension, D 1.35, indicating that clouds are statistically self similar in the horizontal plane. This implies that processes involving clouds have no horizontal length scale over this range (Lovejoy 1982).

It is clear that this horizontal self-similarity must break down as one investigates smaller scales, since the microscopic structure of clouds begins to be dominated by viscous and molecular effects instead of the thermodynamic forcing noted at the macroscopic level. A study of the perimeter- area relation of severe convective clouds in midlatitudes revealed that such a break does exist. Radar returns of intense storm clouds containing hail were observed as they developed and consequently grew in size. At a diametric length scale below three kilometers, a linear fit to the observations, given by Equation (2-1 $P = C \cdot \sqrt[D]{A}$. (2-1), called for D 1.0. This indicates smooth, or nonfractal behavior. For scales above this point, the study found D 1.36, in close agreement with Lovejoy's result (Rys and Waldvogel, 1986). Do all cloud types, then, have a common horizontal fractal dimension above a certain scale length?

15

A study of more than 400,000 cloud base areas indicated that this is not the case. This study was conducted for fair weather cumulus, statocumulus and convective clouds in the intertropical convergence zone, a region where easterly and westerly trade winds converge, which is often marked by large thunderstorms. High resolution cloud scenes (57 to 120 meters) were analyzed from Landsat-3, 4, and 5 data over the Atlantic and Pacific Oceans, as well as the Gulf of Mexico and Mediterranean Sea (Cahalen and Joseph 1989). Cloud reflectivity thresholds for base and top were determined for each scene and applied to each pixel, producing binary, cloud – no cloud images. The perimeter – area relation was determined using a box counting technique for contiguous areas of pixels containing clouds. This technique was applied by cloud type for cloud bases and tops separately. Findings show that the fractal dimension does, in fact, vary by cloud type, with fair weather cumulus clouds exhibiting a clear scale break in fractal dimension at 0.5 kilometers in diameter. In addition, the perimeter fractal dimension was observed to rise with increasing threshold, or height of the cloud. This was attributed to increased turbulence with height, and culminated with a break in scale as the area decreased approaching the cloud top.

This change in fractal dimension with height is to be expected since the atmosphere is horizontally stratified, to a great extent, with pressure and density decreasing by a factor of e^{-1} over a scale height of approximately seven kilometers (Wallace and Hobbs, 1977). For this reason, clouds can be considered self-affine fractals in three-dimensional space. A self-affine fractal scales differently by dimension, that is, horizontal and vertical fractal dimensions differ. (Lovejoy and Schertzer, 1985).

While a complete characterization for all clouds calls for a spectrum of fractal dimensions, one should conclude that clouds can be described as fractals in space. Thus, clouds can be considered multifractal entities described by a range of fractal measures (Feder 1988).

2.1.2 Clouds as Fractals in Time

The concept of fractal dimension has been effectively used to describe the variations of quantities as records in time. It is important to realize that, since spatial and temporal measures differ fundamentally, the extension to four-dimensional space must be described by self-affine fractals (Feder 1988).

Different cloud types exhibit different temporal and spatial characteristics by type. Evolution of cumuliform clouds and their spatial distributions through time is quite different than that of stratiform clouds. This would lead one to expect the characterization of cloud evolution to be multifractal in nature.

An analysis was performed for 1,600 hourly data domains from the climatological and historical analysis of clouds for environmental simulations (CHANCES) database covering a large portion of the Northern Hemisphere, from the Equator to 30 degrees North latitude (Eis et al. 1997). This study showed variations in spatial fractal dimension over the domain consistent with the multifractal nature of clouds already established. It also indicated variation of fractal dimension with percentage of mean cloud cover for varying cloud field distributions. A scatter plot of the data, shown in Figure 2-3, bounds the relationship between cloud cover and fractal dimension. A plot of the fractal

dimension versus time shows significant variation, *0.75 < D < 1.9,* over a 500-hour period.
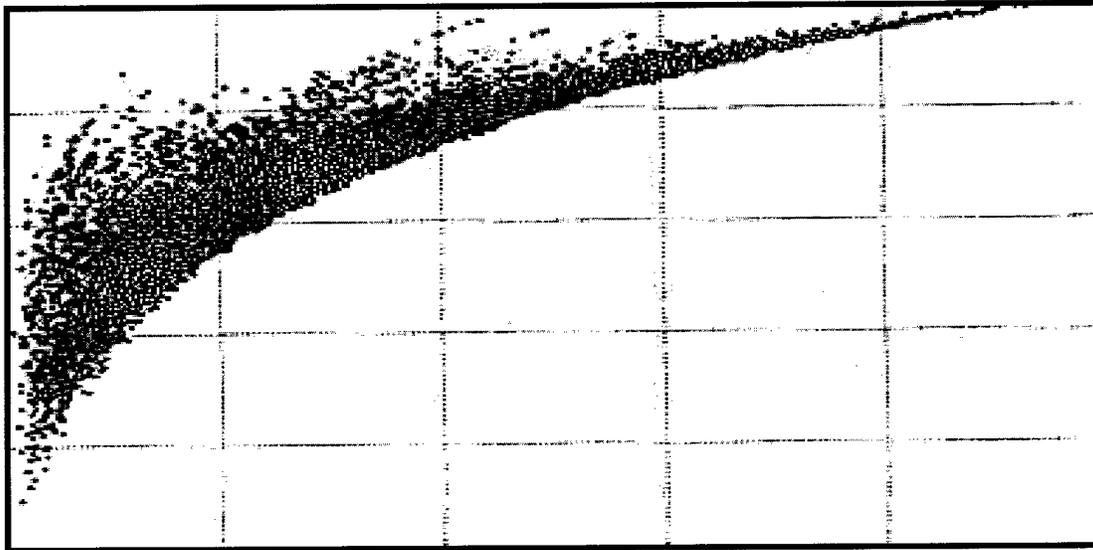
Figure 2-3. Scatter Plot Showing the Variation of Fractal Dimension
versus Cloud Cover (Eis et al. 1997).

The development of a cloud, or a field of clouds, in time is obviously dependent on initial conditions. For it to change shape in time, yet still display a fractal structure in four-dimensional space, there must be some interplay between the time and space scales (Hentschel and Procaccia 1984). This would call for a spectrum of fractal dimensions, again emphasizing that clouds must be modeled as multifractals in space and time.

While average fractal dimensions cannot be used over large temporal or spatial regions, there is evidence that a functional relationship exists between mean cloud cover and fractal dimension for limited times and areas (Eis et al. 1997).

2.2 Re-scale and Add Algorithm

The RSA algorithm is a computationally efficient method for producing random fractals in multiple dimensions (Saupe 1989). It is the core algorithm in the CSSM used to model spatial and temporal characteristics of simulated cloud fields. This algorithm also helps to determine the variability of simulation cloud liquid water content (CLWC) distributions and random convective heating, which drives cumulus cell development in the model. The next section describes use of the RSA algorithm in the CSSM in more detail. Here, we will discuss the algorithm, its features, and its implementation in the CSSM.

The re-scale and add method produces fractal sets by approximating fractional Brownian motion in one or more dimensions (Feder 1988). This involves constructing a multidimensional lattice of Gaussian random numbers having zero mean and the same variance for all points. These random numbers represent individual frequencies, which will be used to construct the fractal field. The lattice is then sampled according to the RSA formula, and the terms are summed to produce a value at each point on the output grid, V(x), which represents the working domain of the cloud field simulation. The RSA formula, as implemented in the CSSM, is given by:

$$V_n(\underline{x}) = \sum_{k=k_0}^{k_1} \frac{1}{r^{kH}} S_n[f(r^k \underline{x}')] \qquad (2\text{-}2)$$

where, n gives the number of topological, or Euclidean, dimensions being modeled; k0 and k1 denote the summation limits for the sampled random terms; H is the Hurst parameter; r is the lacunarity parameter: and Sn[f(rkx')] provides a smooth interpolation

from the random lattice to the output grid position. The RSA formula represents a random function, which has output with a fractal dimension given by:

$$D = n + 1 - H \qquad (2-3)$$

The characteristics of the resultant fractal can be determined by adjusting any of five parameters: the Hurst parameter, the lacunarity parameter, the upper and lower summation limits, and the lattice resolution. The first four parameters are explicitly represented in the RSA equation, while the final parameter, lattice resolution, is a relation between the random lattice and the output grid. A brief description of each parameter's effect on the output field follows.

The Hurst parameter, H, controls the amplitude of each term being sampled from the random lattice, where each term can be thought of as a frequency. Lower frequencies control the large-scale structure of the fractal surface, while higher frequencies provide textural information. Larger values of H cause the amplitude of these frequency terms to decrease more quickly as the summation index increases, causing lower frequency terms to have more influence on the output, while smaller values increase the influence of higher frequency terms. The result, as illustrated in Figure 2-4, is a smoother image with increasing values of H.

H=1.5   **H=3**

H=6   **H=7.5**
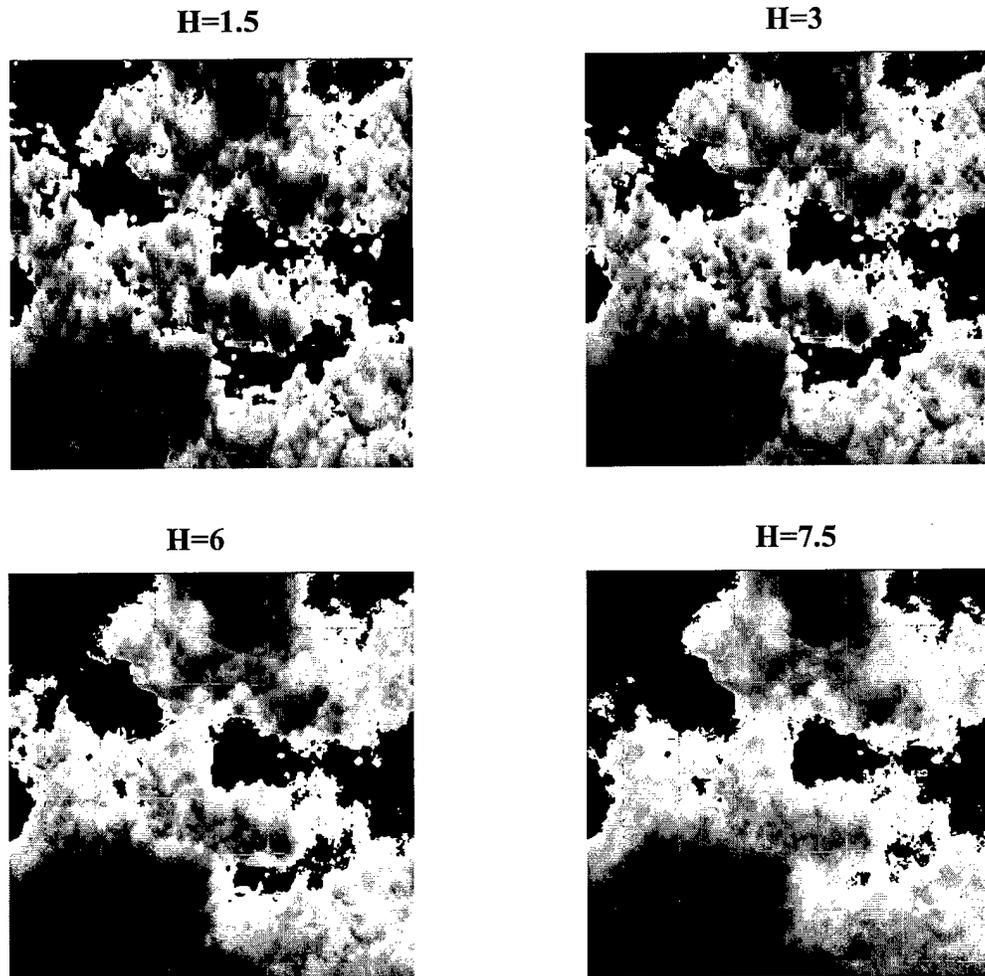
Figure 2-4. Effect of Varying Hurst Parameter (H) on Fractal Field. Increasing
values of H give increasingly smoother cloud fields (Triantifiolo
1998).

The lacunarity parameter, r, appears in two places in the RSA formula. First, it is

used to control amplitude, along with the Hurst parameter, in the term $1/r^{kH}$. Its effect is

similar to, but more subtle, than that of the exponential Hurst parameter. Second, it is

used to determine the location to interpolate from the random lattice, with larger values

of r giving a larger distance between lattice points, and greater textural variability, and

smaller values of r giving less variability. The effects of the lacunarity parameter are

bound with those of the lattice resolution, summation limits, and Hurst parameter in such

21

a way that it is difficult to isolate. In general, small values of r give smoother fractal fields with less small-scale structure, while larger values of r give rougher fields with more detailed small-scale structure, as illustrated in Figure 2-5. It is important to note that although changes in r may make changes in the overall character of the output fractal field they do not change its fractal dimension.

r=1   r=3

r=6   r=9
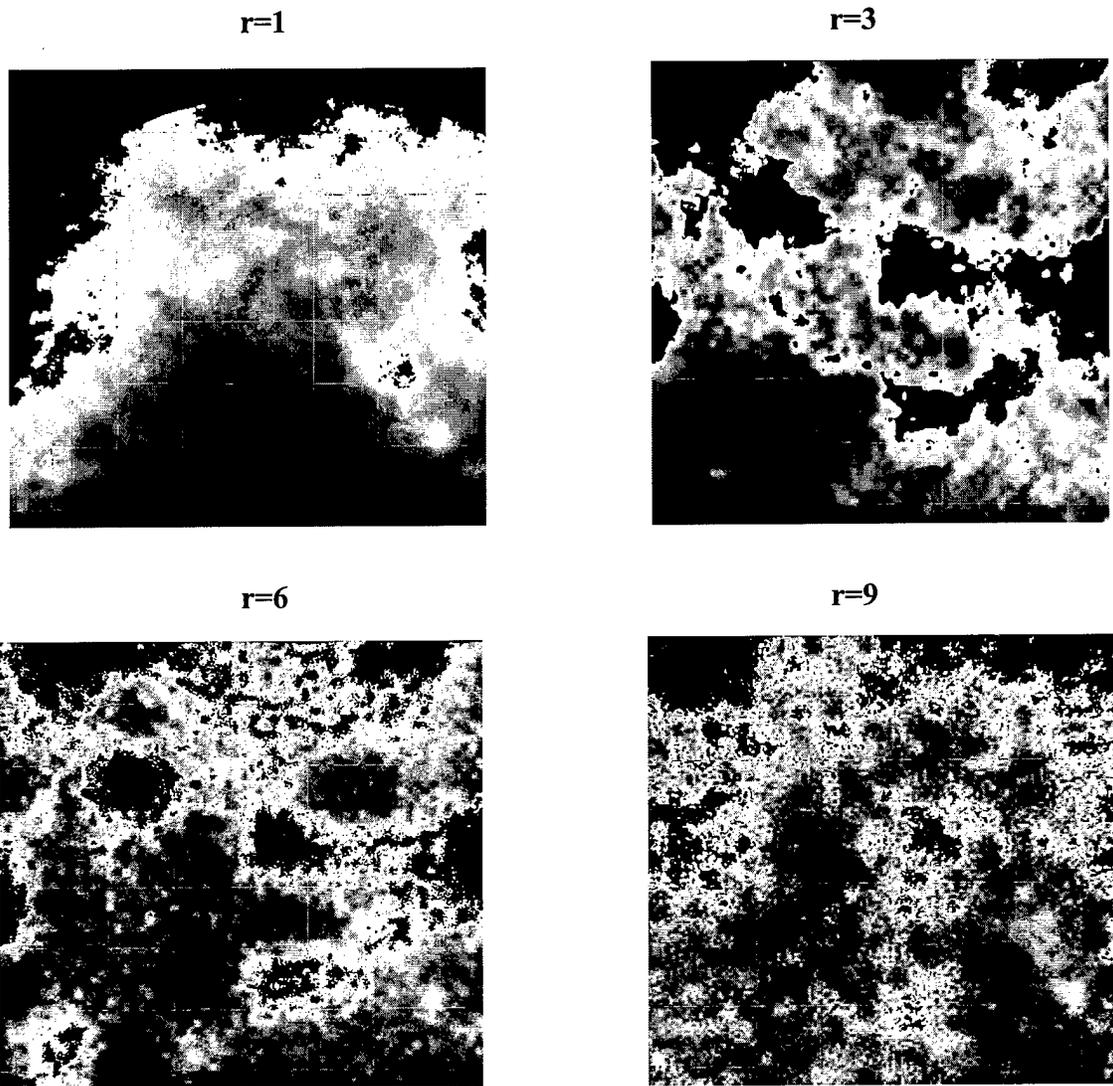
Figure 2-5. Effect of Varying Lacunarity Parameter (r) on Fractal Field. Smaller values of r give smoother cloud fields with less small-scale structure (Triantifiolo 1998).

22

The summation limits in the RSA formula are used to specify the range of spatial dimensions to be represented in the fractal field, with the lower limit giving the largest scale, and the upper limit giving the smallest. A lower summation limit of zero represents frequency terms on the order of the resolution parameter in size that is, having the same resolution as the terms which make up the random lattice, while the upper limit can be chosen to represent frequency terms of the smallest resolution desired. Figure 2-6 shows images for each of five frequency terms, and an image produced by summing those frequencies (Cianciolo and Rasmussen 1992).

K=1   K=2

K=3   K=4

K=5   Total Summation
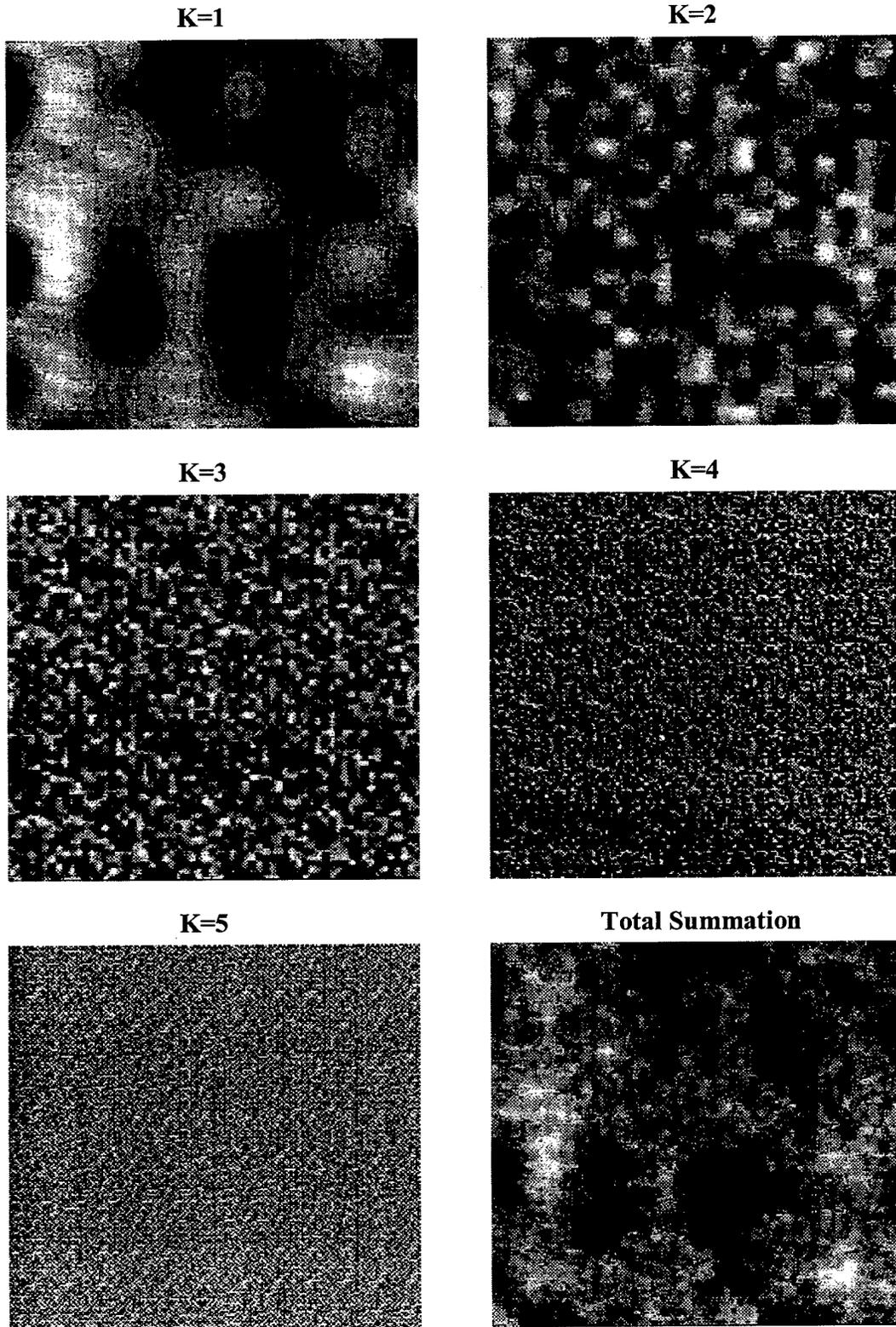
Figure 2-6. Summation Frequencies (K) and Their Combined Effect (Cianciolo and Rasmussen 1992).

The final parameter, lattice resolution, provides the relationship between the random lattice and the output grid for the fractal field. It controls the spatial distribution of fractal field values by determining the number of output grid points for each point in the random lattice. As resolution increases, the number of output grid points per lattice point increases. Consequently, the field becomes smoother for increasing lattice resolution values, as illustrated in Figure 2-7 (Cianciolo and Rasmussen 1992).

Lr=4   Lr=6

Lr=9   Lr=12
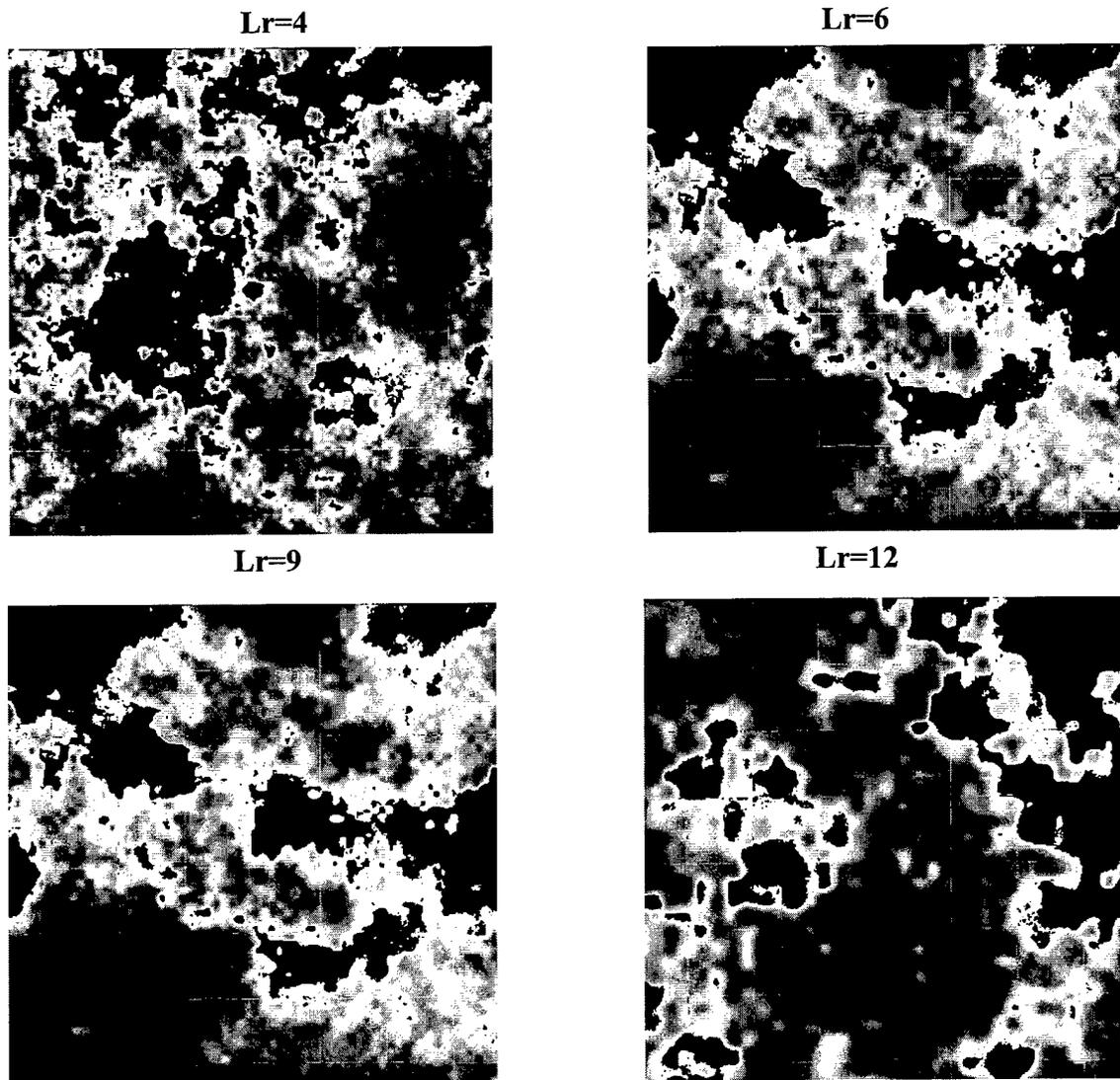
Figure 2-7. Effect of Varying Lattice Resolution (Lr) on Fractal Field. The cloud field becomes smoother as lattice resolution increases (Triantifiolo 1998)..

25

Unlike many random fractal generation techniques, RSA is a pointwise calculation that can be applied to variable-resolution grids. Since no explicit reference to other points is required, the order of computation of fractal points is unimportant. This allows implementation on computer systems with parallel processors, and a significant increase in speed for fractal field generation (Saupe 1989).

2.3   Cloud Scene Simulation Model

This section provides background information about the development of the CSSM. A detailed description of the CSSM will be given, and its method of operation will be discussed.

2.3.1 Background

The CSSM was originally produced to provide multiple high resolution spatial and temporal distributions of CLWC consistent with coarse user input conditions. These cloud fields were then used in radiometric sensor simulations and sensitivity studies in support of the Smart Weapons Operability Enhancement (SWOE) program. Variable-size domains were supported with the capability to incorporate terrain data. Applications using the CSSM were largely limited to stand alone simulations involving scene visualization and sensor evaluation over a small spatial domain for relatively short time periods, 5 to 15 minutes in length (Cianciolo and Rasmussen 1992).

Advanced simulations being developed by the Department of Defense (DoD) modeling community call for high-resolution characterization of the atmosphere in order to increase the realism and accuracy of the simulation environment. These simulations

operate over large-scale domains, often in distributed interactive environments involving numerous simulation models interacting to create a simulated environment for training and testing purposes. The CSSM was enhanced to support such applications requiring interoperability and real time operation. Additionally, the model was modified to accept gridded input meteorological conditions to facilitate coupling with numerical weather models. Adjustment and validation of the spatial parameters was performed by statistical comparison of model output with observational data. Originally, these parameters were estimated based on literature reviews and visual comparison of simulated cloud fields with observed cloud fields (Cianciolo and Raffensberger 1996a).

2.3.2 Description

The CSSM is comprised of 26 programs that work together to produce high-resolution cloud scenes in four dimensions, which are consistent with coarse input meteorological conditions. This is accomplished by using the RSA fractal algorithm, discussed previously, to generate stochastic cloud fields consistent with the input weather conditions. A seed number is specified to initialize the fractal lattice used by the RSA algorithm. By varying the input seed number it is possible to produce a variety of cloud fields consistent with input conditions for use in Monte Carlo studies.

The CSSM contains both a cloud water model and precipitation model. Output from the cloud model consists of three-dimensional grids of cloud liquid water density values, in gm m^{-3}, for each time step of the simulation. The precipitation model produces simulated rain rate values, in mm hr^{-1}, for nimbostratus, cirrus uncinus, and precipitating cumulus cloud types only.

27

The CSSM can simulate 13 specific cloud types including cirriform, stratiform, and cumuliform varieties. Two structured cloud types are also supported, stratocumulus cloud streets, and stratiform orographically driven wave clouds. The model can simulate multiple cloud types concurrently for as many as 12 layers. Table 2-2 lists all cloud types that can be simulated by the CSSM

Table 2-2. Cloud Types Simulated by the CSSM.

Cloud Type	Abbreviation	Remarks
Cirrus	ci	
Cirrocumulus	cc	
Cirrostratus	cs	
Cirrus Uncinus	cn	Uses precipitation model
Stratus	st	
Altostratus	as	
Nimbostratus	ns	Uses precipitation model
Stratocumulus	sc	
Altocumulus	ac	
Cumulus	cu	Uses convective model
Precipitating Cumulus	cp	Uses precipitation and convective models
Stratocumulus Cloud Streets	scs	
Stratus Wave Clouds	stw	

The model typically operates at resolutions from 10 to 100 meters within a user-defined domain. For evolution of the three-dimensional cloud fields in time, the model uses input weather conditions bounding the simulation start and end times. Often, high temporal resolution on the order of one minute is required, and input weather data from forecast model output, or an archived database is available at intervals on the order of one hour. In these cases, the model interpolates coarse weather conditions for intermediate time periods, accomplishing temporal evolution, that is, growth and dissipation of cloud elements, using the RSA fractal algorithm operating in the *time* dimension (Cianciolo and Raffensberger 1996a, b).

2.3.3 Method of Operation

This section will detail the processes used by the CSSM to generate synthetic cloud fields from user-input general conditions. Discussion will proceed in approximate chronological order, as performed by the CSSM, and will cover initial processes common to all cloud types. Following this, processes which are unique to creation of the stratiform cloud types used for the study will be discussed.

2.3.3.1 Initial Processes

The model begins by processing input supplied by the user. This data consists of four types: input parameters, meteorological data, cloud data, and terrain data. The latter three types can be specified as horizontally homogeneous across the simulation domain, or as gridded inputs varying across the domain. Section 3.2 discusses input data format in greater detail and provides examples used in this study.

Once input data has been ingested, the model then interpolates the meteorological and cloud data in time according to the bounding conditions. This interpolation is governed by the TUPDATE parameter, which is set to 5 minutes in the current version of the model. This parameter specifies the time interval between interpolation points. If only initial conditions are provided then they are considered uniform over the course of the simulation and interpolation is not performed.

Wind data, in u and v component form, is first interpolated to determine advection distances for large-scale cloud structures, which are assumed to move with the average wind field. The advection distance is the distance over which these structures move

29

between interpolation points. This interpolation ensures that meteorological conditions vary smoothly through time for lengthy simulations employing input conditions which vary in time.

The CSSM next generates an advection value history for actors joining large-scale simulations after the initial start time. This step is not necessary, however, for stand-alone simulation applications. Using the advection information determined previously, the internal working domain for the model is defined. This domain is larger than the user-specified output domain to account for advection into the output domain during the course of the simulation. The working domain is also increased to ensure continuity across output domains for multiple actors interacting in large-scale simulations using gridded input conditions. In these cases, the working domain is increased in size by at least one half grid box, as determined by the coarse input data, so values interpolated at the output domain boundary can be computed similarly.

If gridded input conditions are specified, they are interpolated to the finer output grid resolution. This is accomplished by means of a bilinear interpolation scheme, and the resultant high-resolution data fields are used to generate the cloud fields.

Next, a horizontal fractal field is generated using the RSA algorithm discussed in section 2.2. A four-dimensional lattice of random numbers is generated using an input seed number. This lattice contains 40x40x10x10 values for dimensions x, y, z, and t in the current version of the model. The RSA formula is evaluated for each grid location to generate a two-dimensional fractal field. This field is constructed at each user-specified cloud base level, with new distributions being generated at a rate determined by

TUPDATE, which is 300 seconds in the current version of the model. Variability of the

fractal field is determined according to the RSA parameters discussed previously, which

have been tuned according to cloud type. These field values are then used to form a

horizontal distribution of cloud elements for each user-specified cloud base layer in the

working domain. This is accomplished by creating a histogram of field values, which are

then used to determine a threshold value for each grid location to produce the amount of

cloud coverage consistent with user input. The general cloud form desired determines the

processes used by the CSSM after this point (Cianciolo and Raffensberger 1996a).

2.3.3.2 Stratiform Cloud Generation

The stratiform cloud model is used to generate cloud fields for all cloud types

according to their RSA parameters, except cumulus and precipitating cumulus clouds.

While the cirriform cloud types do make use of a cirriform cloud model, it is identical to

the stratiform model initially, but does contain additional features to produce cirriform

clouds. The steps followed by the stratiform model are to build cloud bases and tops for

the horizontal fractal distribution of cloud elements already computed. The model then

generates internal water content values for each cloud-filled grid point in the working

domain.

The user-specified cloud base heights are adjusted to exhibit the irregular

bumpiness observed in real clouds. The RSA algorithm is used to generate a stochastic

perturbation field for each cloud-filled grid location according to parameters that have

been tuned for each cloud type. The perturbation used to vary the cloud base height for

each grid point is given by:

31

$$base_{perturbation} = \frac{rsa \cdot base\_percent \cdot (top - base)}{5} \qquad (2\text{-}4)$$

Where *rsa* is the value computed using the RSA algorithm; *base_percent* is a

parameter which determines the overall amount of cloud base variation; *top* and *base*

heights are those specified by the user in the cloud data file. These perturbation values

are added to the nominal base height at each grid point to obtain the simulated cloud

base.

The cloud top is now constructed using the fractal field values calculated to

determine the horizontal cloud distribution with the height of the cloud top being a

function of horizontal field value. This is determined by:

$$top' = base + (top - base) \cdot \left[\frac{rsa - threshold}{1 - threshold} \right]^{1.5} \qquad (2\text{-}5)$$

Where *top* and *base* are those specified by the user in the cloud data file; *rsa* is the

fractal field value computed for the horizontal cloud distribution by the RSA algorithm;

threshold is the cloud-no cloud threshold level computed for the grid location. The

exponent, 1.5, was determined by analysis of real clouds.

Once cloud base and top have been computed, the water content for each cloud-

filled grid point must be calculated. This is given by the sum of the average water

content computed for a particular grid location plus a perturbation value based on RSA

formula values tuned according to cloud type.

The average water content at a grid point is a function of cloud type, cloud

temperature and vertical position within the cloud. A lookup table based on the Feddes

32

synoptic scale model for condensed atmospheric moisture provides values for maximum condensed moisture according to cloud type and temperature (Feddes 1974). The average water content is then calculated as a fraction of this maximum value based on the height of the grid point above the cloud base.

Perturbations are then added to the average water content derived from maximum values given by the Feddes model to produce the small-scale variations in CLWC observed in real clouds. The RSA algorithm is employed once more to produce a field of perturbation values corresponding to each cloud-filled grid point. Parameters are selected to produce simulated clouds consistent with observed ones. Perturbation quantities are produced by scaling these RSA field values by the ratio of the standard deviations of the RSA field values to the standard deviation of the water content for the particular cloud type. Standard deviation values for internal liquid water content were determined empirically by analysis of observed cloud water data, where available. These values were estimated for cloud types where no data were available for analysis.

Once perturbed water content values have been calculated for all cloud-filled grid points, all grid points with values of CLWC less than two standard deviations below the average for the cloud are set to zero. This introduces small cloud-free spaces inside the simulated cloud field, similar to that observed for real clouds (Cianciolo and Raffensberger 1996a).

2.4   Fast Map Postprocessor

The Fast Map postprocessor to the CSSM was developed to generate optical, radiative and graphical quantities needed to render realistic three-dimensional cloud

images from CSSM output files (Cianciolo and Raffensberger 1996a; Raffensberger et al. 1996). Note that the Fast Map processor itself does not generate or render graphical images. Instead, it uses a series of analytic process to provide physically based values to a graphical scene-rendering engine. This enables scenes to be generated quickly enough to support high-speed real-time interactive simulations, which must produce approximately 13 images per second to maintain a convincing real-time environment. The Fast Map processor was used to produce volumetric grids of optical quantities corresponding to CSSM CLWC files, which were then used to derive the radiometric time series used for the CSSM validation study. This section provides operational details about how the Fast Map processor generates these grids, and briefly describes the approach used to obtain graphical quantities.

The mapping of CLWC to optical properties begins by first developing spatially varying particle size distributions for each grid location inside the cloud. Using this particle size distribution information, optical properties are calculated. This includes extinction optical depth and single scattering albedo for both visible (.55μm) and near infrared (11μm) wavelengths. Next, tables mapping the optical values to radiative properties are constructed. These are based on radiative transfer model calculations and parameterizations derived from observational research. Finally, a wavelength-dependent mapping is made between radiative properties and graphical quantities used to render visual images of the CSSM clouds. The construction of a database of two-dimensional tables relating cloud water content to cloud type, particle size, optical properties, radiative properties and graphical quantities is key to the Fast Map postprocessor's speed. While the Fast Map processing approach is similar for all cloud types supported,

implementation varies by cloud type due the various parameterizations required. Steps in the Fast Map process leading to the production of the optical properties used in the study will now be described in more detail.

In order to readily develop the spatially varying droplet size distribution for each CSSM grid location, the distribution is discretized into narrow radius bins. A modified gamma distribution is assumed to describe the number density for all cloud types according to particle size. Thus, the number density at grid point i, j, k over a radius size range r_l to r_{l+1} is given by:

$$n_l(i,j,k) = \int_{r_l}^{r_{l+1}} n(r)dr \qquad (2\text{-}6)$$

Where the modified gamma distribution is:

$$n(r) = ar^{\alpha}e^{-br} \qquad (2\text{-}7)$$

The parameters α, a, and b vary by cloud type according to those developed for use in the LOWTRAN and FASCODE two-stream radiative transfer models, as given in Table 2-3.

Table 2-3. Parameters used for droplet size distributions by cloud type (Cianciolo and Raffensberger 1996a).

Cloud Type	α	b	a
Cumulus	3.000	0.500	2.604
Stratus	2.000	0.600	27.000
Stratocumulus	2.000	0.750	52.734
Altostratus	5.000	1.111	6.268
Nimbostratus	2.000	0.425	7.676
Cirrus	6.000	1.500	0.011865

Spatial variation of the particle size distribution must be introduced to accurately model a cloud's physical, optical and radiative properties. The Fast Map processor assumes a linear variation of number density from cloud base to cloud top, and adjusts the modified gamma distribution accordingly. Variation with horizontal location is not addressed, and so, number density is considered horizontally uniform. While these simplifications are not completely physically accurate, they are considered a reasonable first-order approach for this first-generation version of the Fast Map processor.

Particle size information for each cloud type is given by statistical averages derived from real cloud observations. The number density in each particle size bin is then derived from the local liquid water content at each grid location and the average liquid water content for the particular cloud type. Once the local number density has been calculated for each grid point, this information is summarized in two-dimensional tabular format. Since the distribution is known, only the maximum and minimum values are stored for each size bin. This greatly reduces the amount of memory required for each cloud field and increases speed.

At this point, the cloud microphysical properties have been specified. Now the optical properties, particularly extinction optical depth and single scattering albedo, are determined. This is accomplished using a data set of lookup tables containing values for the extinction and scattering coefficients. These values were precomputed for wavelengths between 0.25µm and 14µm over a fixed set of size bins falling within the modified gamma distribution. Output quantities from the Fast Map postprocessor are given for visible wavelengths, centered on .55µm, and for infrared wavelengths, centered

on 11μm. Recall that the observational data used for this study was collected by a normal incidence pyrheliometer sensitive to radiation in the interval 0.3μm and 3μm.

The extinction optical depth gives the attenuation of radiance along a path due to absorption and scattering. This value is obtained by multiplying the extinction coefficient by the path length through the particular grid location for each size bin, i, according to:

$$\delta_i = \Delta L_i \cdot \sigma_{extinction\,i} \qquad (2\text{-}8)$$

Since this value scales linearly with droplet number density, only the minimum and maximum values of optical depth are retained for each size bin. Extinction optical depth can then be calculated by linear interpolation between these values for each grid location (Cianciolo and Raffensberger 1996a).

Grids of extinction optical depth values provided by the Fast Map postprocessor were used to facilitate radiative transfer calculations needed to derive radiometric time series data from the cloud scene model output. Chapter 3 will describe this process in detail.

2.5   Cloud Forcing of Radiometric Traces

The signature of cloud forcing on radiometric time series traces can be used to infer information about cloud field spatial structure and its evolution through time. This thesis applies this method to time series produced by the CSSM as a means of evaluating its temporal performance

A proof of concept study established the validity of this approach to analyze the spatial structure of cloud fields passing between a ground-based pyranometer and the sun (Seeley et al. 1997). Optically thick clouds in a field of broken sky coverage, and advecting in the direction of the mean wind at cloud level caused variable attenuation of the signal observed at the pyranometer. For relatively constant wind speed, variation of the solar cosine signal observed for clear-sky situations reflects spatial structure of the cloud field over the pyranometer as the field advects and evolves with time.

Spectral analysis of the pyranometer data was used to characterize the spatial structure of the cloud field. Analyses of a wide variety of cloud data, from satellite imagery to in-situ measurements, has revealed a decay of the spatial fluctuations in Fourier space according to the power law:

$$E(k) \propto k^{\beta} \tag{2-9}$$

over a spectrum of length scales from 0.5 to 20km. These studies have determined β to be in the range $-1.4 < \beta < -2.0$, and provides a benchmark for the study. Examination of several pyranometer time series extracted from the experimental data set revealed a similar power law decay, with the spectral exponent in the range $-1.4 < \beta < -2.4$.

Also included in the data set was radar data for the sky over the pyranometer. The radar data consisted of reflectivity values capable of revealing vertical cloud structure up to 60,000 feet. Integration of these reflectivity values provided another measure of the spatial and temporal variation of the cloud fields. Spectral analysis of this data also reveals a power law dependency having spectral exponent values consistent with the pyranometer data (Seeley et al. 1997).

Results of Seeley's work indicated that analysis of radiometric time-series

signatures is a valid approach for studying cloud field spatial structure for broken cloud

cover and steady wind.

3. Methodology

In this chapter, the techniques employed to accomplish this temporal study of the Cloud Scene Simulation Model (CSSM) will be described. This includes processing of real data, model initiation and production of simulated time series.

3.1 Processing of Real Data

Data for this study were provided by the Air Force Phillips Laboratory. These data was part of a larger data set resulting from the ACT/EOS validation experiments conducted at Hanscom AFB, Massachusetts (Hiett 1995).

3.1.1 Data Description

The data were collected from 10 to 13 July 1995. The data set consisted, in part, of standard meteorological information collected by a Vaisala Milos 500 weather station located on the test site. This information included radiance values measured by a normal incidence pyraheliometer mounted on a solar-tracking device. This instrument is sensitive to radiation in the visible and near infrared wavelengths from .3 to 3μm. Also included in the data set were time lapse images of the sky above the test site. These images were taken by a closed circuit television camera during the entire period and digitized at one-minute resolution. The cloud movies provided a detailed record of cloud types and sky conditions over the test site, which were time indexed to other data in the set. Information about cloud base and top heights was provided by the TPQ11 cloud profiling radar. This vertically pointed radar is located approximately 1,000 feet from the

test site, and is capable of measuring clouds as high as 62,000 feet at a resolution of 75 meters. Ancillary meteorological information was also included, which consisted of atmospheric sounding information collected each morning at 1200 UTC, as well as surface observations from numerous weather stations in Massachusetts. All data, with the exception of the ancillary data and cloud movies, were collected at one-minute resolution, synchronized to a common time index, and stored in netCDF database format.

3.1.2 Processing of Real Data

Initially, 18 case studies were selected by viewing cloud movies over the test site for 11 and 12 July 1995. These cases exhibited broken to overcast sky coverage for stratiform cloud types, and ranged from 35 to 60 minutes in length. Subjective analyses established predominate cloud types and percent sky coverage representative of each study. This information was later used to initialize the CSSM.

Radiometric time series, corresponding to the time of each study was then extracted from the data set. These data were used to provide information about the evolution of the cloud field over the test site with time, and were compared with simulated time series data produced from cloud fields generated by the CSSM. Additional information needed to accurately initialize the cloud scene model was also extracted from the data set.

Information provided by the TPQ-11 was of primary importance in establishing the height of cloud bases and tops for each cloud layer over the test site. These data were stored as time-indexed, binary reflectivity information. Figure 3-1 shows an example vertical reflectivity time series for 11 July 1995. Each time series frame is 170 minutes

41

in duration with the first beginning at approximately 1330 UTC. The horizontal lines are height markers placed in increments of 3,000 feet. Notice the development of a two-layer cloud system in the second frame. The TPQ-11 data enabled accurate modeling of these features, both spatially and with time. When cloud bases were very low ground clutter returns obscured the cloud-base height information. During these times, observations from nearby weather stations were consulted to establish cloud base heights. This height information, along with cloud type and sky coverage information obtained from analysis of the cloud movies, was used to initialize the CSSM cloud condition input files for each case study, as discussed in section 3.3.
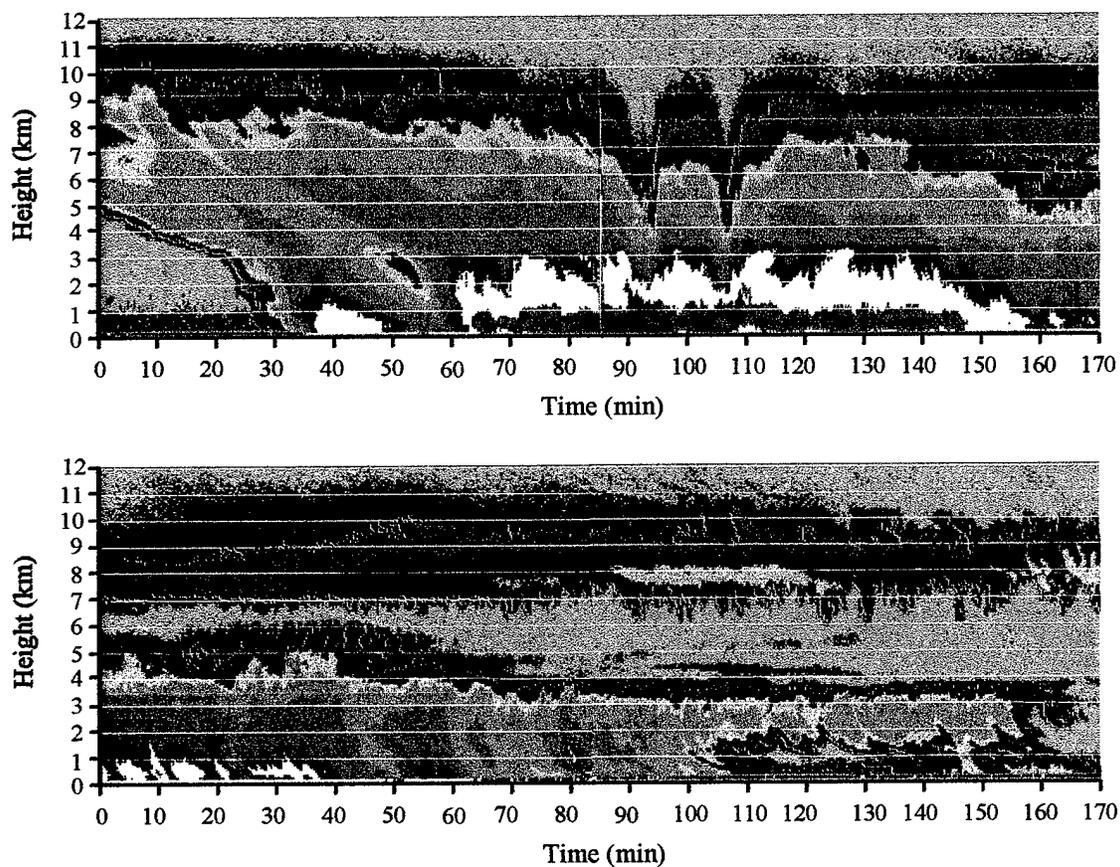
Figure 3-1. TPQ-11 Radar cloud reflectivity time series showing vertical reflectivity over the ACT/EOS test site versus time.

Upper air conditions were furnished by daily atmospheric soundings. These soundings included pressure, height, temperature, relative humidity and wind information at high vertical resolution (three to five feet) throughout the troposphere. Data for only the lowest 10 kilometers of the atmosphere was retained, as stratiform clouds for all study cases were below this level.

Since the CSSM can be initialized with meteorological information for as many as 100 levels, this data was further reduce to 99 layers, approximately one every 100 feet. It was then converted to the proper format for use by the CSSM; see Appendix A for details about this conversion. Surface conditions corresponding to the time of each case study were then combined with the upper air data to produce the meteorological initialization files. The CSSM could then be initialized with this information,.

3.2 Model Initialization

The CSSM requires four types of initialization data to operate: input parameters, meteorological conditions, cloud data and terrain data (Cianciolo and Raffensberger 1996b). The input parameter data specifies all simulation setup parameters. Meteorological data is used to describe the atmosphere so that realistic clouds will be formed and advected through the simulation domain. Cloud data gives the CSSM information to create appropriate cloud coverage at levels defined by the user. Finally, terrain data is used to drive cloud formation. Each data type will now be described more fully.

The input parameter file contains all simulation setup information. Here, simulation start time and duration are specified. The simulation domain and resolution

are defined in space and time. Information about the other three input data types is also contained in this file. Flags may be set to determine what products are output by the model and its mode of operation. The seed number used to initialize the random number lattice used by the re-scale and add (RSA) algorithm is also contained here. Table 3-1 shows an input file for cloud study ten, and provides a summary of the input parameters.

All simulations for this temporal study were conducted at one-minute resolution, to match that of the observed data. A cubical simulation domain was defined to include all stratiform cloud layers for each case study. This required domains which were ten kilometers per side for all cases used in the study. Each domain was defined to have a uniform grid resolution of 100 meters, a nominal value for CSSM applications. The length of each time series study was determined by the cloud conditions observed over the test site. Rapid transition to scattered or clear sky conditions often marked the end of a time series. Studies on the order of one hour were selected, where possible. These studies did not overlap in time in order to reduce correlation among separate studies.

Input meteorological conditions are used by the CSSM in four key areas. Wind speed and direction for each layer are used to specify advection of cloud fields through the simulation domain. Temperature and dewpoint profiles are used to determine the lifting condensation level used in the cumulus model. Together, the input meteorological conditions define the atmospheric stability, which affects cloud street and wave cloud types. However, this study does not use the cumulus, cloud street, or wave cloud types. Input conditions are also used in conjunction with the water content look-up tables to determine cloud liquid water content (CLWC) for all cloud types.

Table 3-1. Example Input Parameter File

Parameter	Description
1995	simulation domain start time: year
7	simulation domain start time: month
11	simulation domain start time: day
17	simulation domain start time: hour
15	simulation domain start time: minute
0	simulation domain start time: second
1995	joining domain start time: year
7	joining domain start time: month
11	joining domain start time: day
17	joining domain start time: hour
15	joining domain start time: minute
0	joining domain start time: second
../data_cld/study10_cld_	root filename of input cloud data
1995	cloud data start time: year
7	cloud data start time: month
11	cloud data start time: day
17	cloud data start time: hour
15	cloud data start time: minute
0	cloud data start time: second
1	frequency of input cloud data files (minutes)
1	number of cloud data files
../data_met/study10_met_	root filename of input met. data
Single	type of input met. data (single or gridded)
1995	met. data start time: year
7	met. data start time: month
11	met. data start time: day
17	met. data start time: hour
15	met. data start time: minute
0	met. data start time: second
1	frequency of input met data files (minutes)
1	number of input met data files
../data_ter/hanscom_elev	root filename of input terrain data
Single	type of input terrain data (single or gridded)
../output/test10.0	root name of output files
454848	number seed used to initialize fractal lattice
1	output gridded water content (1=yes, 0=no)
0	output precipitation rate (1=yes, 0=no)
0	interoperability (1=yes, 0=no)
0.1	x resolution of output domain (km)
0.1	y resolution of output domain (km)
0.1	z resolution of output domain (km)
1.0	t resolution of output domain (min)
10.0	x extent of output domain (km)
10.0	y extent of output domain (km)
10.0	z extent of output domain (km)
45.0	t extent of output domain (min)
0	real-time domain origin (1=yes, 0=no)
0.0 0.0 0.0 0.0 0.0	domain origin (x, y, z,(km), t (min since start)

Input meteorological data can vary at each grid point in the simulation domain, and during the course of the simulation. The scope of this study did not require gridded input files. Instead, meteorological conditions were assumed to be uniform at each level for the entire simulation domain, which covered ten cubic kilometers. A single input file provided initial conditions, and the RSA algorithm was used to determine cloud element evolution throughout the remainder of the simulation run.

The input file consists of one plain text entry for each level, with each entry giving values for pressure in millibars, geometric height above the surface in meters, temperature and dewpoint in degrees Celsius, and u and v wind components in meters per second (where u is positive to the East, and v is positive to the North). Table 3-2 shows an extract of the input meteorological conditions file used for study ten.

Table 3-2. Example Input Meteorological Parameter File.

Pressure(mb)	Height(m)	Temp(°C)	Dewpoint(°C)	U-Wind(m/s)	V-Wind(m/s)
1007.7	0	19.8	16.8	-2.5	0.9
996.6	110	18.1	15.6	0.0	0.0
973.0	310	16.4	15.3	0.0	0.0
959.5	430	15.7	14.3	0.0	0.0
951.8	500	15.6	13.3	-0.4	0.3
938.8	620	15	12.4	-1.0	0.8
289.0	9600	-41.3	-66.2	13.2	17.4
284.9	9700	-42.1	-66.8	13.9	18.8
280.0	9810	-42.4	-65.7	15.4	22
275.7	9920	-43.2	-66.4	16.5	24.3
272.2	10000	-44.1	-67.7	17.3	25.4

Cloud input data files define the large-scale cloud features to be modeled by the CSSM. These include cloud type, fractional sky coverage, mean base and maximum height information for each cloud layer. The CSSM accepts cloud input data in either single format, where cloud conditions are considered homogenous throughout the

46

simulation domain, or gridded format, where cloud conditions can vary through the simulation domain. Here again, the scope of the study called for single input format, though some cases required multiple levels or cloud types. However, no more than three cloud layers and two cloud types were used for any one study.

Cloud layer information was ascertained by assimilating data from a variety of sources. The cloud movies, described in section 3.1.1, provided primary information about cloud types and sky coverage for each study. TPQ-11 radar data, atmospheric soundings and meteorological observations from surrounding areas were used to determine cloud layer base and height information. Subjective analysis and synthesis of this data provided a basis for the cloud input data file, which represented the large-scale cloud features characteristic for each given study. Table 3-3 shows an example cloud input data file for study ten. This plain text file first specifies all cloud types by layer, then provides percent sky coverage, mean base height and maximum top height in meters for each corresponding cloud layer.

Table 3-3. Example Input Cloud Condition File.

Layer	Cloud Type	% Coverage	Base(m)	Height(m)
1	Stratocumulus	40	400	600
2	Stratocumulus	80	1500	3500
3	Stratus	90	7500	9000

The terrain data input file provides surface elevation data to the CSSM, which is used for cloud forcing and stability calculations, as well as lifting condensation level calculations. Terrain data files can be specified as either gridded or single format. The small domains used for this study, between five and ten square kilometers over relatively flat terrain, allowed a single format input file to be used. For all cloud studies, a simple

47

file containing a single value, 90.0, was used to give the elevation of the test site above sea level in meters (Cianciolo and Raffensberger 1996b; T. Hiett 1998, personal communication).

3.3 Simulated Time Series Production

Once the CSSM had been initialized for a particular cloud time series study, it was run for ten different random seed number values, generating ten series CLWC files for the simulation output domain. Each output file contained 1,000,000 gridded data points, representing the simulated atmosphere for each time step. Table 3-4 lists the seed numbers used for each study.

Table 3-4. Seed numbers used to initialize the CSSM.

Seed	Number
0	454848
1	88464
2	554645
3	453602
4	430492
5	1668
6	932704
7	364906
8	254836
9	719726

CSSM files for each time series study were then used by the Fast Map post processor to generate gridded volumes of slant path optical depth values at the same spatial resolution as the CSSM files. Output files for both visible (.55μm) and infrared (1μm) wavelengths were produced by default. The .55μm files were used to derive the simulated time series data, however, since the observed radiometric data being used for

comparison was collected by a pyraheliometer sensitive to wavelengths from .3 to 3μm. The 11μm files were simply discarded to conserve computer disk space.

A ray tracing routine then integrated the slant path optical depth values for each time step in each time series study to obtain a total extinction value for a ray passing through the cloud volume. The following subsection describes the ray tracing routine in more detail. A brief discussion of the radiative transfer theory employed to derive the radiometric time-series will then be provided.

3.3.1 Ray Tracing Through the Cloud Volume

The ray tracing routine iteratively read each Fast Map output file in a time-series, and integrated the extinction optical depth values, which were obtained through bilinear interpolation of the gridded values at each level along the ray path. This ray path was traced from a point at the base of the simulated cloud field volume representing the location of a virtual pyraheliometer, through the volume, toward the position of the sun. Output consisted of extinction optical depth time series information indexed to solar position and Fast Map output file number for each time step. This information was then used to obtain radiance values.

An ephemeris program calculated the position of the sun for the coordinates of the test site and time of each particular study. This information, reported as azimuth and elevation above the local horizon, was updated each minute to simulate the sun's path through the sky. This approach was consistent with the collection of the observed data, where the pyraheliometer recorded normal radiance values each minute as it tracked the apparent motion of the sun. The accuracy of these directional values, for each study, was

49

verified by comparison with those provided by the United States Naval Observatory Astronomical Applications Department (USNO 1999). In all cases the values were found to be in close agreement.

Use of the ray tracing routine for the simulated case studies exposed a consideration not accounted for initially. Weather conditions for both of the two days from which data was selected consisted of broken to overcast sky cover throughout the morning, lasting until mid-afternoon. After this time, skies became scattered and the stratiform cloud types, which were the object of the study, were no longer present over the test site. Consequently, case studies for each day were selected sequentially, beginning shortly after sunrise until mid-afternoon. The early morning radiometric measurements were very small in magnitude, as might be expected under overcast skies. Simulated cloud fields initialized for these conditions produced no extinction values, however, when processed by the ray tracing routine.

Inspection of the CSSM output files verified that cloud fields consistent with the input data had been produced. The time of the case study caused the problem. For early morning studies, the appropriate solar vector traced a path beneath the cloud base, which exited through a side of the output volume before reaching the height of the cloud base. Calculations confirmed that for studies on 11 July 1995 during times when the elevation angle was less than 61°, the solar vector did not exit through the top of the cloud volume. By moving the position of the simulated radiometer this minimum angle could be reduced to 42°, corresponding to 1230Z for the date and location of the test site. Since valid comparison of real and simulated time series could not be accomplished for times

earlier than this, four case studies were omitted from the temporal study. Similar analysis for cases on 12 July 1995 led to four more case studies being dropped.

4.   Data Summary and Analysis

This chapter presents the simulated time series data derived from the Cloud Scene Simulation Model (CSSM) cloud liquid water content (CLWC) fields. This data will be compared, both qualitatively and statistically in order to determine whether CSSM cloud field time series faithfully reproduce temporal variations in observed data. Qualitative analysis of the data was accomplished through description and comparison of time series radiance plots as well as histograms showing the distributions of radiance values for each time series. The statistical methods used to analyze the data were applied in both the temporal and frequency domains. Specifically, the autocorrelation function was calculated from the data to obtain autocorrelation coefficients for each time lag in the series, and small scale variability was analyzed using the variogram. A power law analysis was performed for each log-log plot of frequency versus power. A description of these methods will be given following a discussion of time series analysis and stationarity. Then, the data for each case study will be presented and analyzed.

4.1   Time-Series Analysis

There are two general approaches to time series analysis: time domain methods, and frequency domain methods. Analyses conducted in the time domain characterize the data in the same space in which they are collected. Frequency domain analyses seek to represent the data in terms of contributions to the variation of the data values for a spectrum of time scales, or frequencies. For this reason, these analyses are called spectral analyses (Chatfield 1984; Wilks 1995).

52

The primary objectives of this time series analysis were description of each time series, and comparison of the observed data with the ensemble of simulation time series. Each series was discrete in that radiance values were sampled or simulated at equal time intervals (Chatfield 1984).

The time series analysis methods used required stationarity of the data. This implies that the statistical properties of the time series are independent of the absolute time. Different intervals within the overall series have the same mean and variance, or equivalently, there is no appreciable trend in the mean, or systematic change in the variance over the course of the time series (Jenkins and Watts 1968).

Radiometric time series are not generally considered stationary series, since they exhibit diurnal and seasonal variation. The diurnal non-stationarity arises due to the trek of the sun across the sky and is a function of time and local latitude. This effect on the observed radiance, L, can be approximately described by:

$$L = A \cdot \cos^2 \phi \qquad (4\text{-}1)$$

where A specifies the amplitude, and ϕ is the local latitude. Seasonal variations occur due to Earth's tilted axis of rotation, as it orbits around the Sun.

Two approaches may be taken to convert a time series to stationarity. The first is to transform the data in such a manner that approximate stationarity is achieved. For example, this can be accomplished by subtracting the characteristic cosine of the sun, as given in Equation (4-1), from the radiometric time series. Another method involves subtracting a value computed as the running mean for each time step. The second

approach is to stratify the data being analyzed. That is, separate analyses are conducted on subsets of the data for intervals short enough that near-stationarity can be reasonably assumed (Wilks 1995).

Data stratification was the primary approach taken in this validation study to approximate stationarity of the time series data. Studies ranged in length from 45 to 60 minutes. Since the focus of this study was stratiform clouds under overcast conditions, the sun's characteristic cosine signature did not readily appear in the radiometric time series.

4.2   The Autocorrelation Function

The autocorrelation function is an important tool used to characterize the properties of time series data in the time domain. This funnction measures the correlation between successive data values in the time series as a collection of autocorrelation coefficients. The correlation coefficient between x_t and x_{t+1} can be computed according to:

$$r_1 = \frac{\sum_{t=1}^{N-1}(x_t - \overline{x}_{(1)}) \cdot (x_{t+1} - \overline{x}_{(2)})}{\sqrt{\sum_{t=1}^{N-1}(x_t - \overline{x}_{(1)})^2 \cdot \sum_{t=1}^{N-1}(x_{t+1} - \overline{x}_{(2)})^2}} \qquad (4\text{-}2)$$

where $N\text{-}1$ is the number of data point pairs in the discrete time series. Here $\overline{x}_{(1)}$ is the mean of the first $N\text{-}1$ data points, and $\overline{x}_{(2)}$ is the mean of the last $N\text{-}1$ observations. This formula, which is commonly simplified by taking these means to be approximately equal,

54

can be extended to find the correlation between observations a discrete distance k apart in time. This gives the computational form of the autocorrelation function (Chatfield 1984, Wilks 1995):

$$r_k = \frac{\sum_{t=1}^{N-k}(x_t - \overline{x}) \cdot (x_{t+k} - \overline{x})}{\sum_{t=1}^{N}(x_t - \overline{x})^2} \qquad (4\text{-}3)$$

Once the set of autocorrelation coefficients has been calculated, they can be plotted as a function of time lag. This graph, called a correlogram, can then be used to analyze and compare time series. The first coefficient in this series will always be $r_0=1$, since the data will be perfectly correlated with itself initially. Other coefficients fall within the range $-1 < r_k \leq 1$. Significantly correlated data can be determined with approximately 95% level of confidence according to limits defined by the equation:

$$l \cong \frac{\pm 2}{\sqrt{N}} \qquad (4\text{-}4)$$

The time of first zero crossing of the autocorrelation functions is used to infer a correlation length scale with time (Turkington et al. 1998).

4.3   The Variogram

The variogram is a time domain method used to analyzed variability in the radiometric signal over short time scales. This is accomplished by determining the magnitude of the difference between the value at a particular time step and an average value for the three time steps centered on the one under consideration. Variability values

are computed in this fashion for each time step of the time series according to the formula:

$$\mathrm{var}(t_i) = \sum_{i=1}^{N-1} \left| \frac{(r_{t-1} + r_t + r_{t+1})}{3} - r_t \right| \qquad (4\text{-}5)$$

r is the radiance at time t. A plot of the observed and simulated radiance values with time enables small-scale variability to be readily compared.

4.4 Power Law Analysis

Power law analysis is a frequency domain method used to succinctly describe structure in terms of power law decay or growth of fluctuations in Fourier space, that is, contributions to the variations in a time series, which occur over a spectrum of different frequencies or time scales. These contributions have been widely observed to have a power law dependency according to (Seeley et al. 1997; Davis et al. 1996):

$$P \propto k^{\beta} \qquad (4\text{-}6)$$

In order to perform the power law analysis, it is necessary to first express the variations in the time series data as a sum of sine and cosine components. This is done by means of the Fourier transform, given by:

$$c_j = \frac{1}{\sqrt{n}} \sum_{k=1}^{n-1} v_k e^{i\left(\frac{2 \cdot \pi \cdot j}{n}\right)k} \qquad (4\text{-}7)$$

where n is the total number of elements, k, in the time series. The result is a sum of terms representing the complex amplitudes of the various frequencies in the original time series data. From these, the power spectrum can be determined according to:

$$P = |c_j|^2 \qquad (4\text{-}8)$$

The power spectrum represents the contribution to the variability, in this case of the radiometric time series, with frequencies in the range $(f_k, f_k + df)$.

The frequency corresponding to each element, k, in the sum can be determined using:

$$f_k = \frac{j}{n} f_s \qquad (4\text{-}9)$$

where f_s is the data sampling frequency with dimensions of minute^{-1} for this study, and n is the number of samples in the time series. Note that the lowest frequency corresponds to variations for only a single cycle over the entire length of the time series, $f_1 = n^{-1}$, while the highest frequency, referred to as the Nyquist frequency is the highest frequency with meaningful information. This is the frequency of variation over only two time intervals in the data series, 2 minutes for this study. Due to limitations imposed by the Nyquist frequency, power spectrum data corresponding to frequencies above this limit, which arose as part of the fast fourier transformation, were eliminated from the data set prior to calculating the power law exponent (Wilks 1995).

Taking the logarithm of both the frequency and power spectrum terms, we may plot the power spectrum as a function of frequency to determine the exponent, β, in the

power law equation, (4-6). This exponent is given by the slope of a linear least squares fit to the data plotted according to:

$$\log P(f) = A - \beta \cdot \log f \tag{4-10}$$

where A is simply a constant corresponding to the zero-crossing of the frequency axis for the fit line (Davis et al. 1996). Comparison of the observed and simulated data sets can then proceed as a comparison of the best-fit slopes to the log frequency versus log power plots.

4.5   Presentation and Analysis of Data

This section will present the observed data for each temporal study along with a representative selection of corresponding simulation data, generated according to the methods described in Chapter 3. Analysis of this data will be accomplished according to the methods outlined at the beginning of this chapter.

Of the 18 case studies originally selected from the data, 8 early-morning cases were eliminated during the ray tracing portion of the project as mentioned in Section 3.3.1. Four more cases were eliminated because the clouds being modeled were too optically thin, and the cloud coverage too sparse for the ray tracing process to be effective. Optical depth time series produced for these cases were largely zero values. Several attempts to shift the location of the virtual pyranometer in the simulated cloud volume were made in order to sample a more optically thick region. While these efforts weren't successful, they did highlight limitations of this validation method.

4.5.1 Study 1

Study 1 was conducted over a 60 minute period for initial cloud conditions listed in Table 4-1. The time of this study was from 0946 to 1046 EDT. There were 2 stratus cloud layers with no appreciable separation between them. The lower layer was precipitating and was easily distinguished from the upper layer with TPQ-11 radar imagery, since the precipitating layer had a much higher reflectivity. Mean wind for the lower layer was 4 m/s, and the mean wind for the upper layer was 9.4 m/s. Advection of the cloud layers is governed by the mean wind for each layer.

Table 4-1. Cloud Layer Information for Study 1

Layer	Cloud Type	Sky Coverage (%)	Base (m)	Top (m)
1	ns	100	300	3000
2	st	100	3000	8500

Examination of the observed radiometric trace in Figure 4-1 (A) shows small-scale variability associated with the varying optical thickness of the cloud passing between the sun and the pyranometer as it advects and evolves with time. Radiance magnitudes are small, corresponding to both the overcast situation and the low elevation angle of the sun. The histogram of radiance values in Figure 4-1 (B) shows a wider distribution of values than those for the simulation data. Figure 4-1 (C) shows the correlogram which, indicates first zero-crossing at 10 minutes for the observed data, and in (D) the power law analysis gives $\beta = -4/3$.

Comparing the observed data to the simulation data, given in Figure 4-2 and Figure 4-4, it is apparent that more small scale variation exists in the observed data than in the simulation data. The variograms for study 1, shown in Figure 4-3 and Figure 4-5,

59

also support this conclusion. There is a wider range of radiance values for the observed

data, the zero-crossing time is longer, and the power law slope is steeper. These results

held for all simulation runs for study 1.
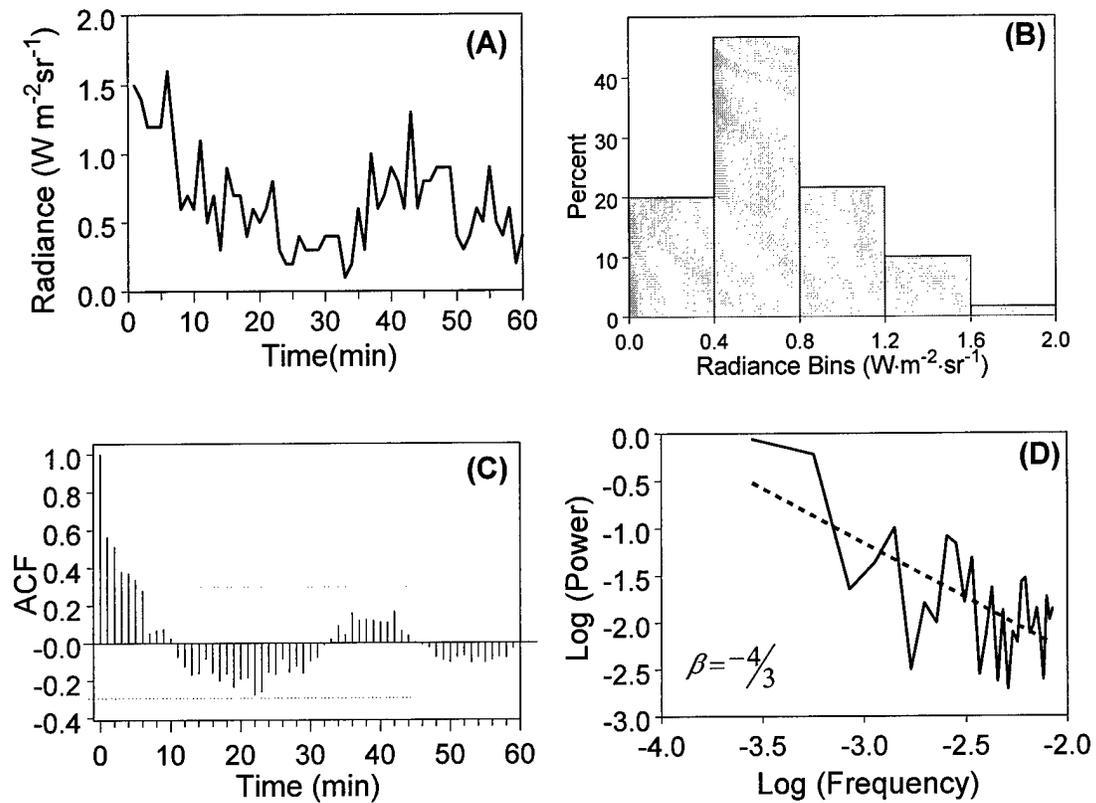
Figure 4-1. Study 1 Observed Data: (A) Radiance Time Series (B) Histogram
(C) Correlogram (D) Power Spectrum.
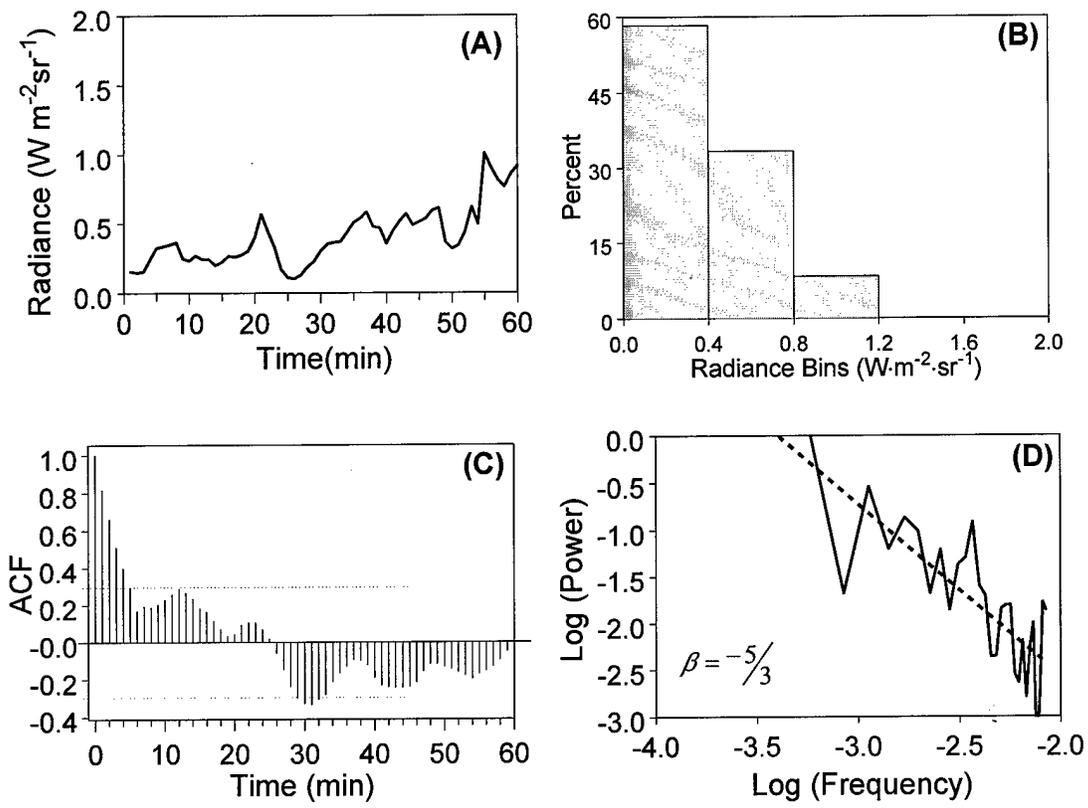
Figure 4-2. Study 1 Simulation 3 Data: (A) Radiance Time Series (B) Histogram (C) Correlogram (D) Power Spectrum.
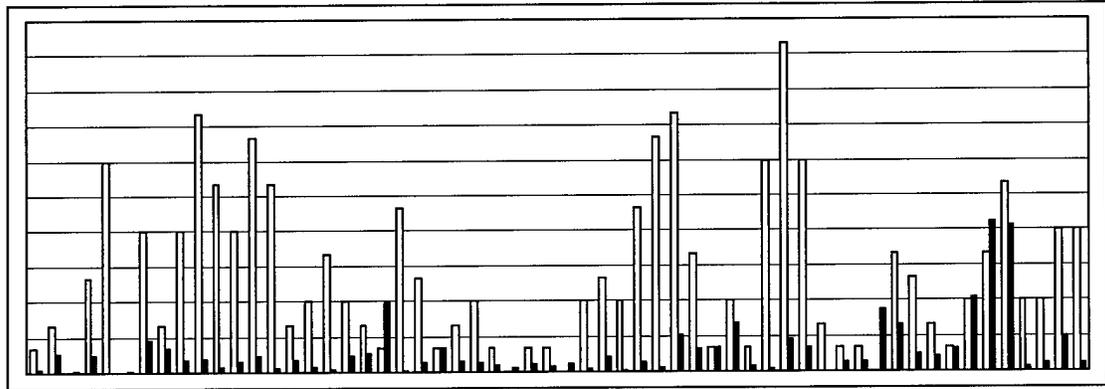
Figure 4-3. Variogram comparing Study 1 variability for a stratus/nimbostratus case. The light colored bars are for observed data and the dark bars are for Simulation 3 data. The observed data exhibits a higher degree of small-scale variability than the simulation data.
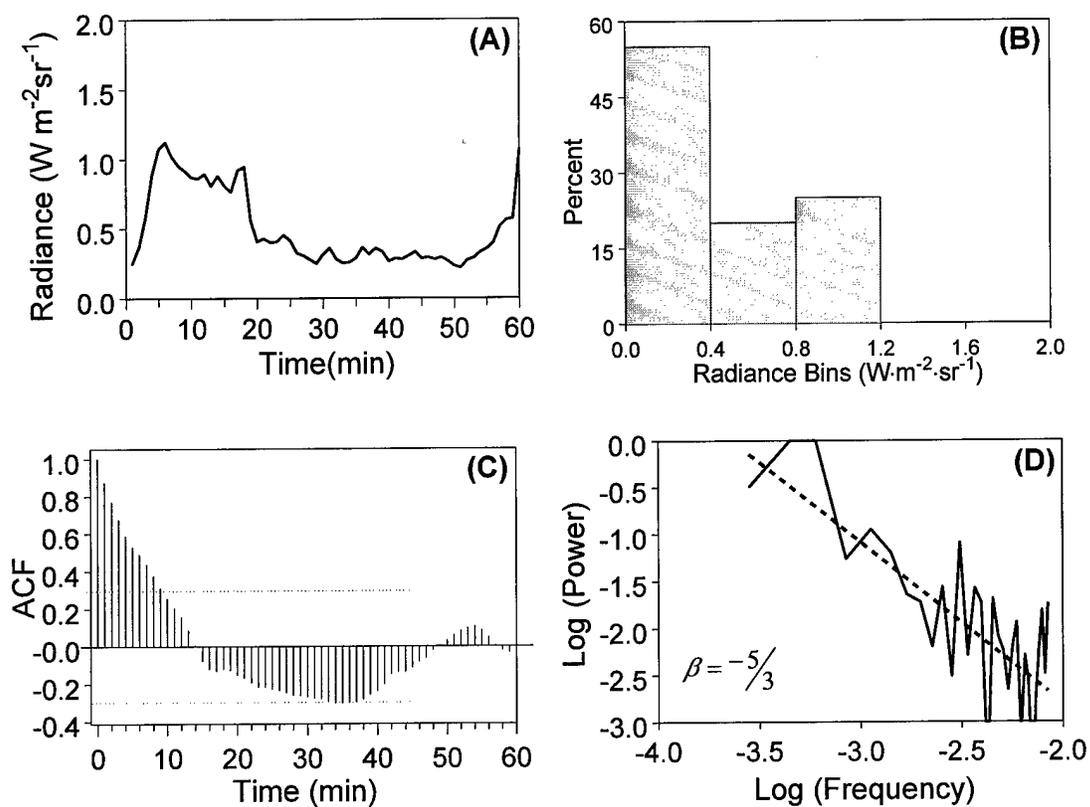
Figure 4-4. Study 1 Simulation 4 Data: (A) Radiance Time Series (B) Histogram
(C) Correlogram (D) Power Spectrum.
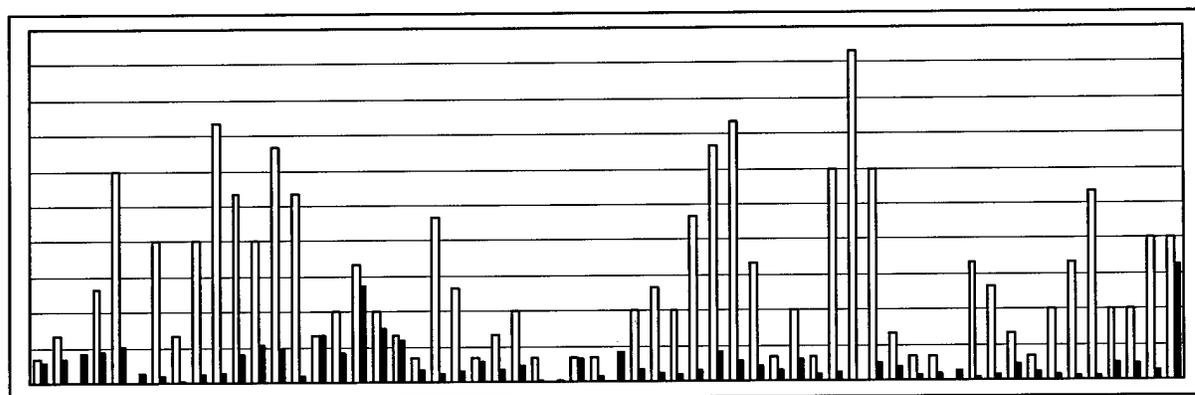
Figure 4-5. Variogram comparing Study 1 variability for a stratus/nimbostratus
case. The light colored bars are for observed data and the dark bars
are for Simulation 4 data. The observed data exhibits a higher
degree of small-scale variability than the simulation data.

62

4.5.2 Study 2

Study 2 was conducted for the 60 minute period following study 1. The two cloud layers persisted, with the lower one still precipitating and no separation between the layers. Cloud information used for this study is given in Table 4-2. Mean wind in the cloud layers was the same as that for study 1.

Table 4-2. Cloud Layer Information for Study 2

Layer	Cloud Type	Sky Coverage(%)	Base(m)	Top(m)
1	ns	100	300	3250
2	st	100	3250	8250

This case study is similar to study 1 in that the simulation radiometric traces did not exhibit the degree of small scale variability observed in the real data. Radiance value distributions represented the range of the real data better for this case study than for study 1. The simulation distributions were generally skewed toward smaller radiance values for the simulations than for the observed data. The time scale correlation results as given by the correlogram were ambiguous in that the observed zero-crossing occurred at 10 minutes, while simulation zero-crossings occurred above and below this value. Power law analyses showed simulation slope values to be greater than real values for this case study. Compare Figure 4-6 (D), 4-8 (D), and 4-9 (D). This confirmed the notion that more contribution to radiometric signal variability occurred for low frequencies, or long time scales for the simulation time series than for the observed data. More small-scale variability in the simulation data would have given a greater contribution to the power spectrum at shorter scales, and a correspondingly shallower slope. Inspection of

63

the variograms for all simulation runs also indicated a greater degree of small scale

variability for the observed data as illustrated in Figures 4-8 and 4-10.
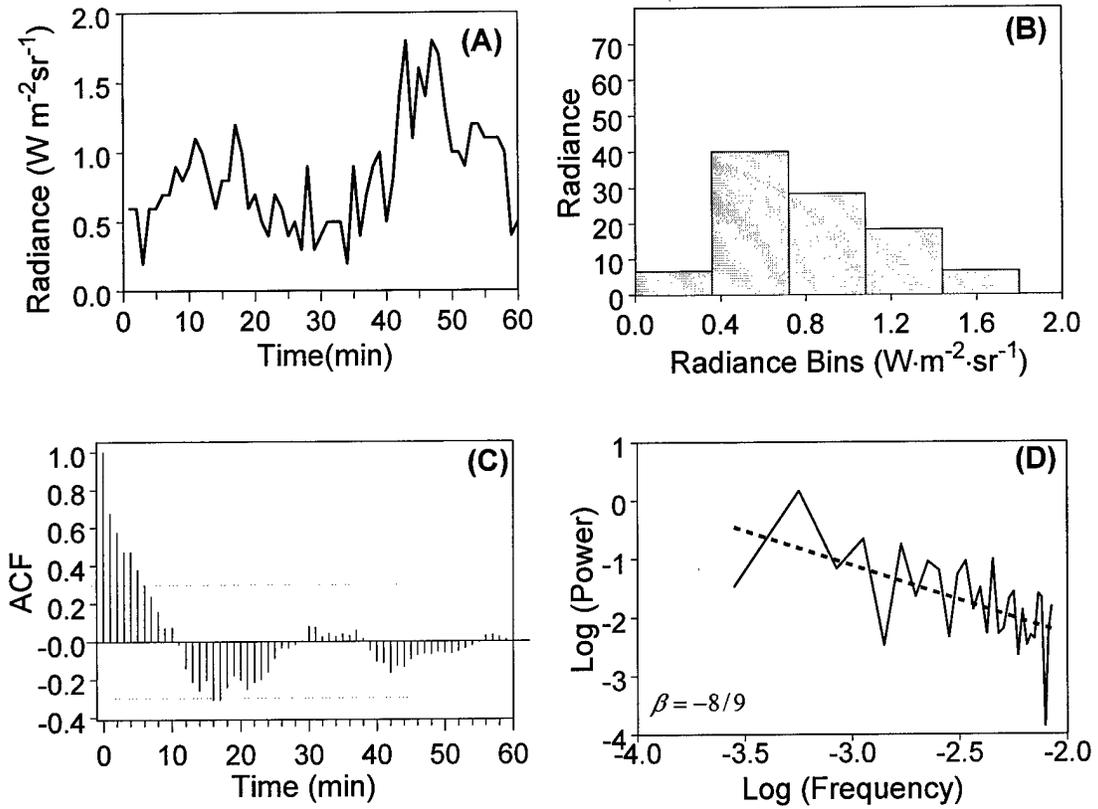
Figure 4-6. Study 2 Observed Data: (A) Radiance Time Series (B) Histogram (C) Correlogram (D) Power Spectrum.
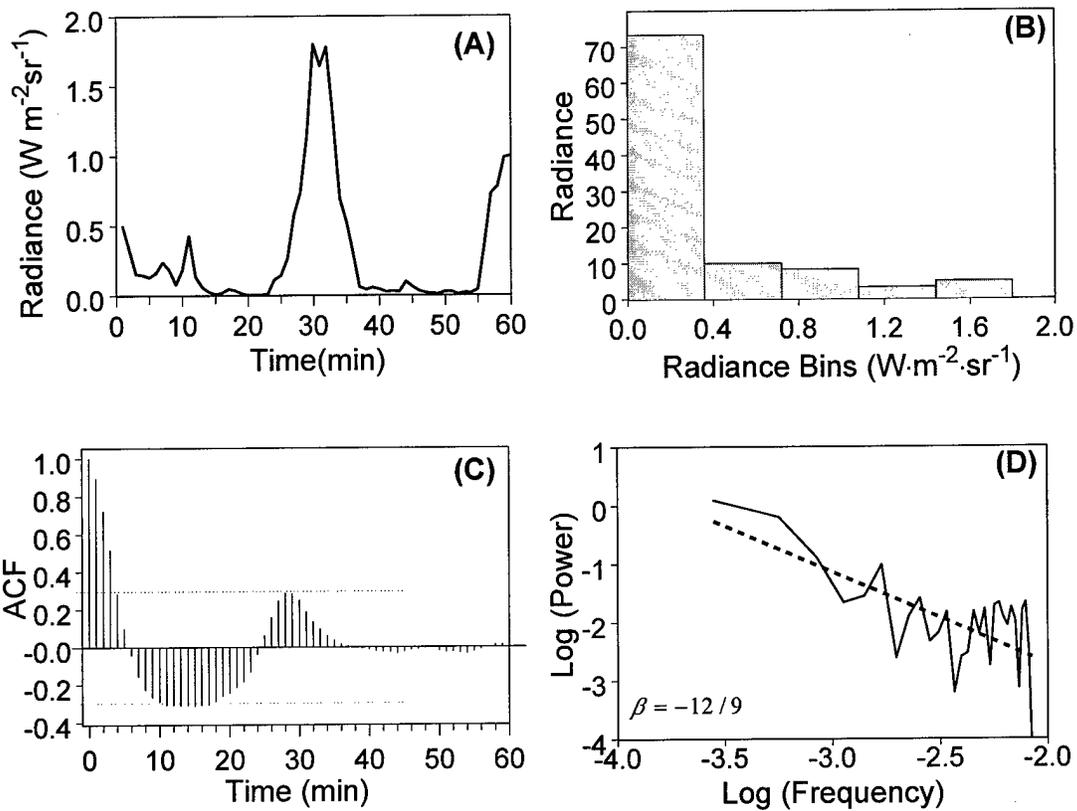
Figure 4-7. Study 2 Simulation 5 Data: (A) Radiance Time Series (B) Histogram
(C) Correlogram (D) Power Spectrum.
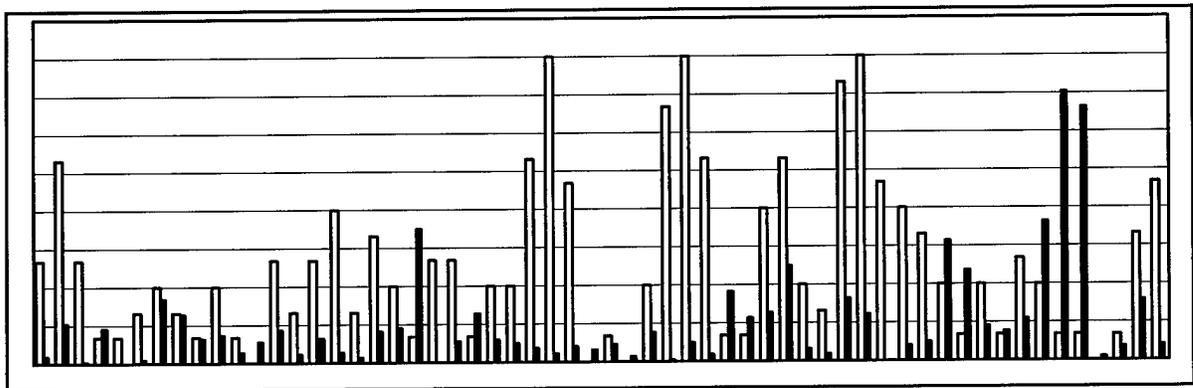
Figure 4-8. Variogram comparing Study 2 variability for a stratus/nimbostratus
case. The light colored bars are for observed data and the dark bars
are for Simulation 5 data. The observed data exhibits a higher
degree of small-scale variability than the simulation data.
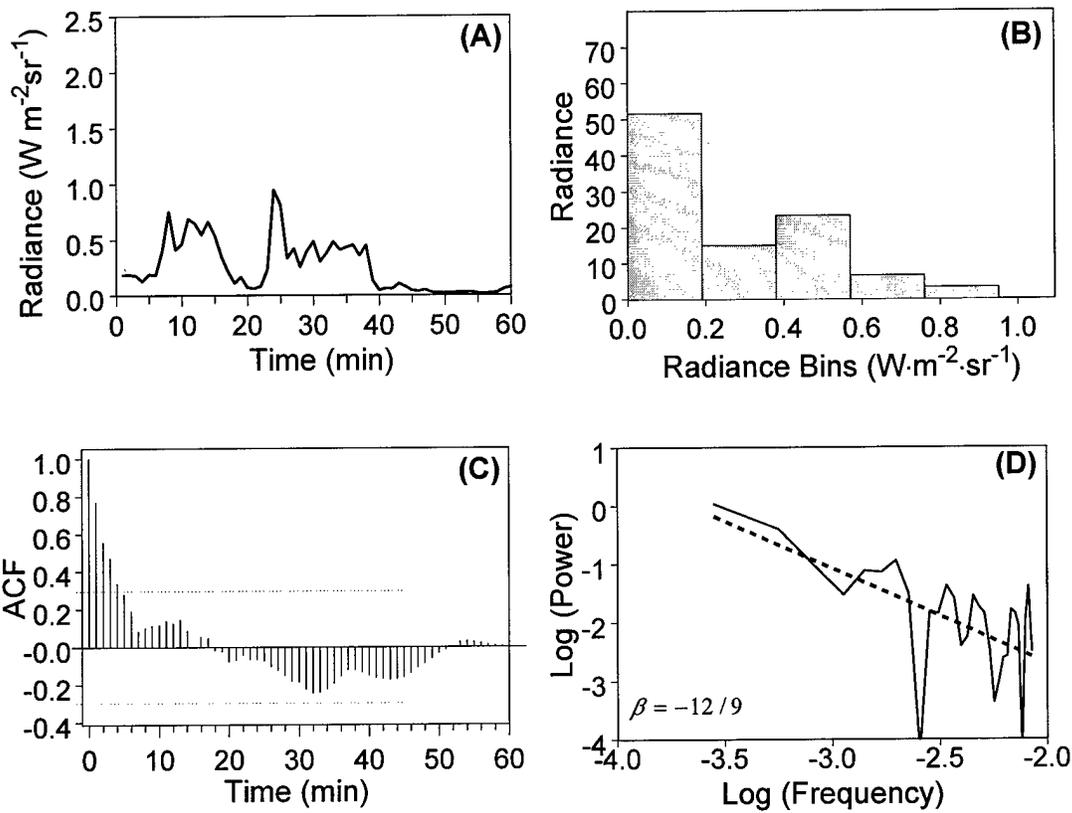
Figure 4-9. Study 2 Simulation 7 Data: (A) Radiance Time Series (B) Histogram
(C) Correlogram (D) Power Spectrum.
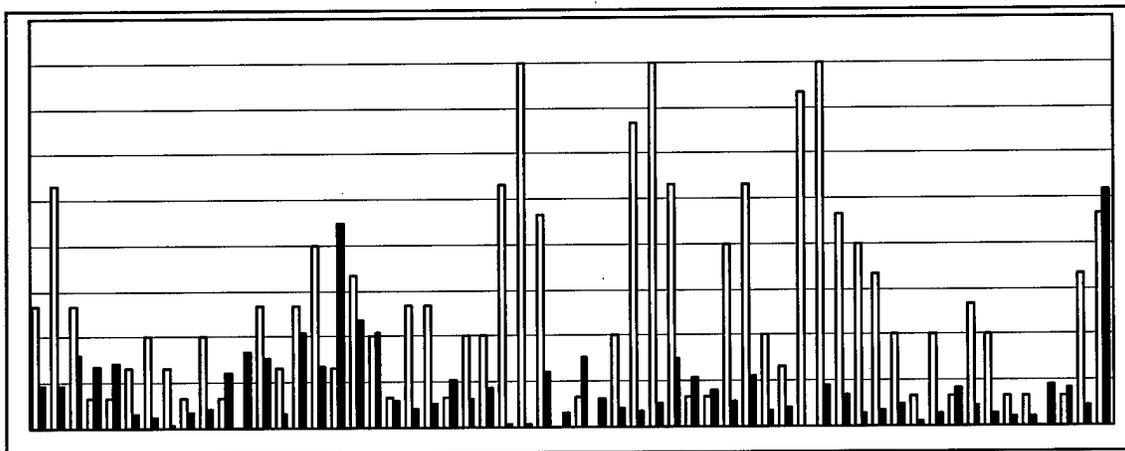
Figure 4-10. Variogram comparing Study 2 variability for a stratus/nimbostratus
case. The light colored bars are for observed data and the dark bars
are for Simulation 7 data. The observed data exhibits a higher
degree of small-scale variability than the simulation data.

4.5.3 Study 3

Study 3 simulated a 60 minute period following the precipitation in case studies 1 and 2. The two cloud layers present earlier continued. However a vertical separation developed between the cloud layers. The mean wind in lower layer was 5.8 m/s, while the mean wind in the upper layer was 11.1 m/s. Table 4-3 gives the bases and heights of these layers as well as the percentage of cloud sky coverage.

Table 4-3. Cloud Layer Information for Study 3

Layer	Cloud Type	Sky Coverage(%)	Base(m)	Top(m)
1	st	90	400	5000
2	st	90	7250	8000

A subjective analysis of the radiance time series in Figure 4-11 (A) and comparison with corresponding simulations in Figure 4-12 (A) and Figure 4-14 (A) shows significant differences in the character of the signatures. The observed data again exhibits a highly variable signature, indicating a cloud field that was highly variable with time. The simulation data shows a less variability with time, corresponding to less variability in the cloud field elements with time. Histograms show the observed data to have a wider distribution of radiance values over the course of the time series than the simulation data. Correlation time scales for the simulation data were shorter than that for the observed data, which had a zero-crossing time of 19 minutes. Zero-crossing times were approximately half that of the observed data for all simulation runs in this case study. Results of the power law analyses were not conclusive since the observed data gave a power law relationship that sometimes had a steeper slope than the simulation data. Other times, the simulation data gave a steeper slope than the observed data. Cases

where the observed slope was steeper than that for the simulation data provided a counterintuitive result, given that the observed data shows more small-scale variability. Variograms for all simulations showed that small scale variability was not as evident in the simulation data. Figures 4-13 and 4-15 provide comparisons with observed data for simulations two and three, respectively.
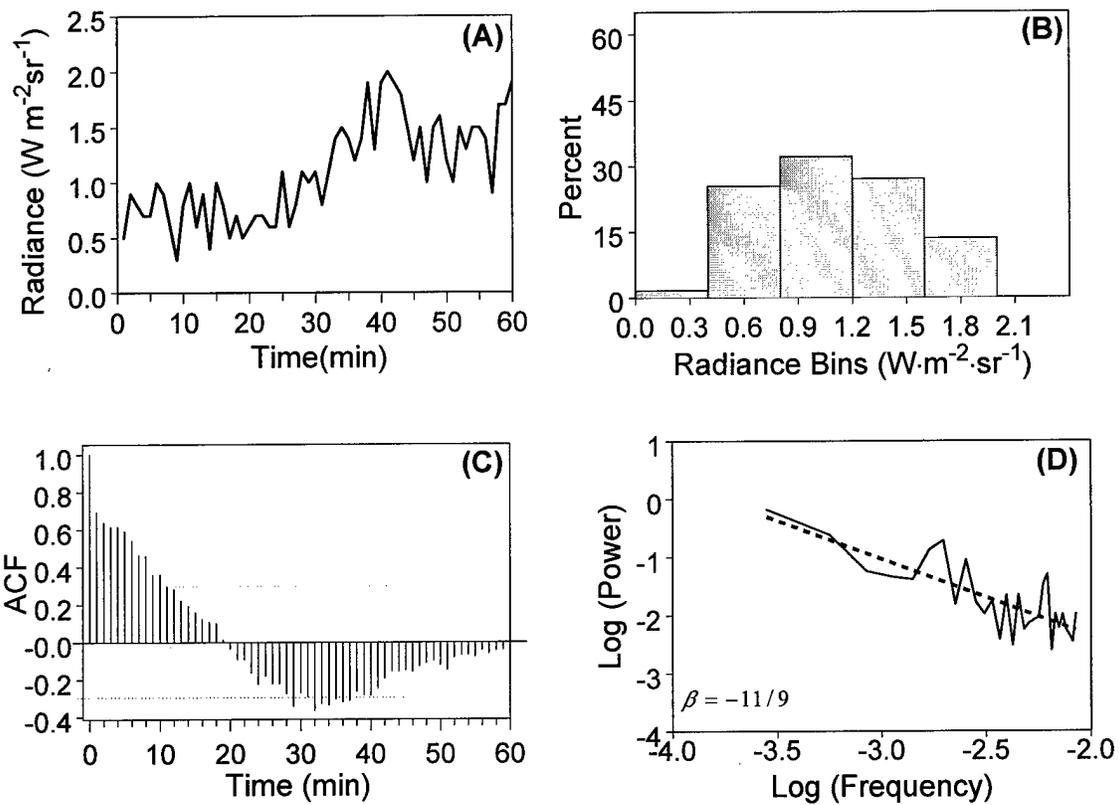
Figure 4-11. Study 3 Observed Data: (A) Radiance Time Series (B) Histogram (C) Correlogram (D) Power Spectrum.
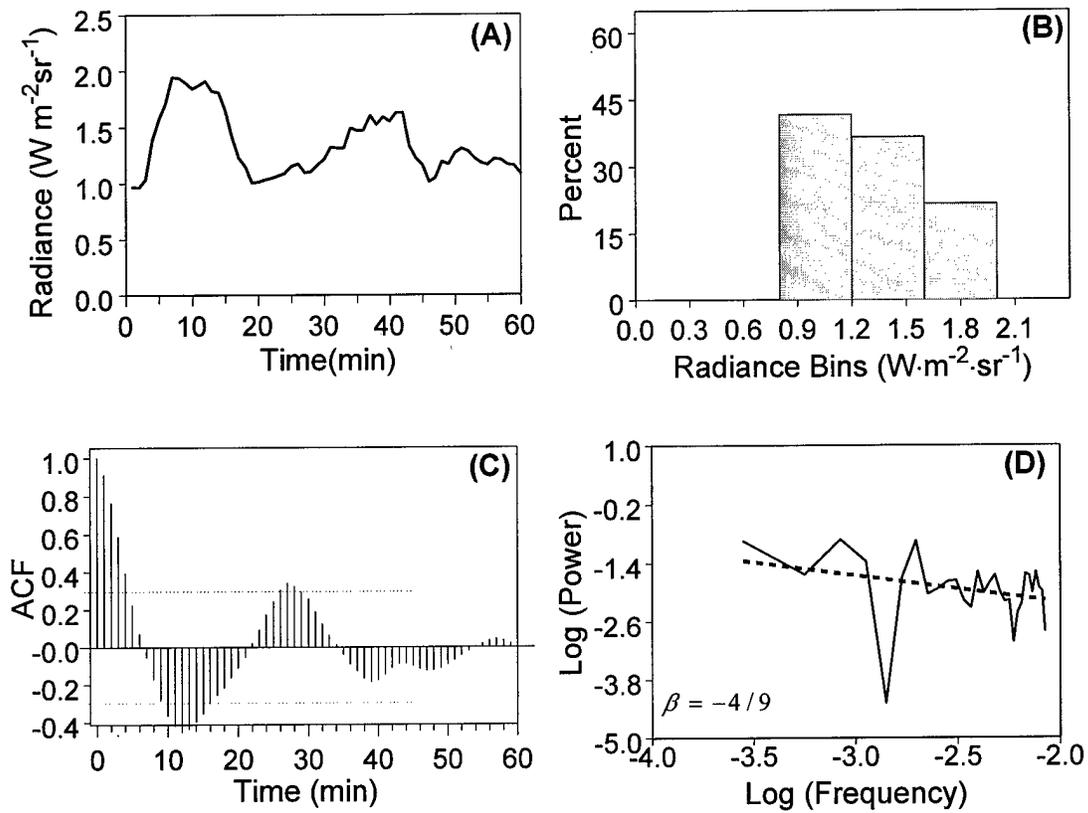
Figure 4-12. Study 3 Simulation 2 Data: (A) Radiance Time Series
(B) Histogram (C) Correlogram (D) Power Spectrum.
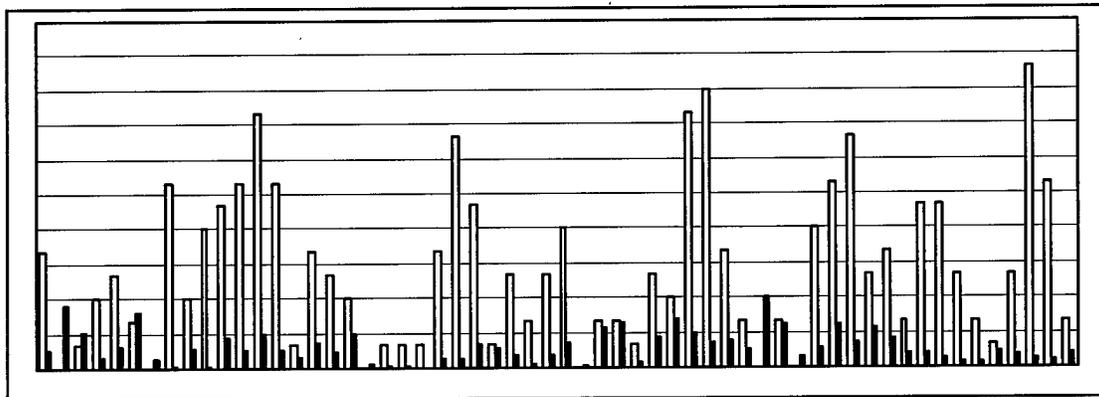
Figure 4-13. Variogram comparing Study 3 variability for a stratus case. The light colored bars are for observed data and the dark bars are for Simulation 2 data. The observed data exhibits a higher degree of small-scale variability than the simulation data.
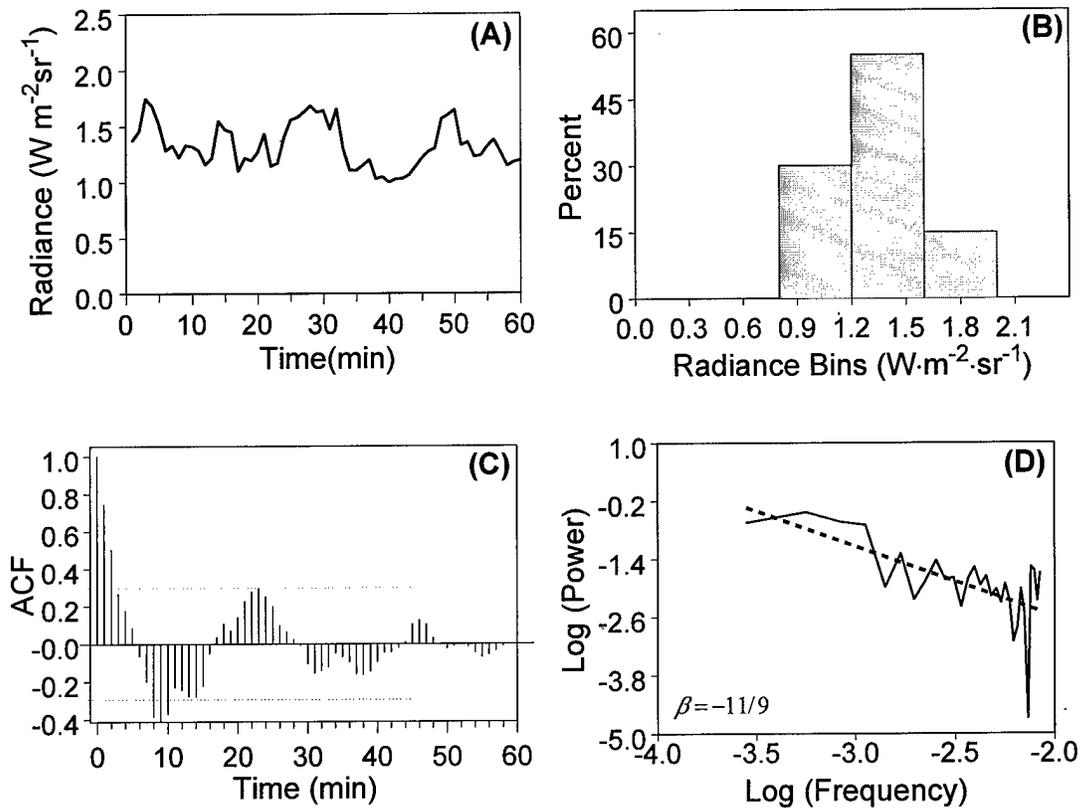
Figure 4-14. Study 3 Simulation 9 Data: (A) Radiance Time Series
(B) Histogram (C) Correlogram (D) Power Spectrum.
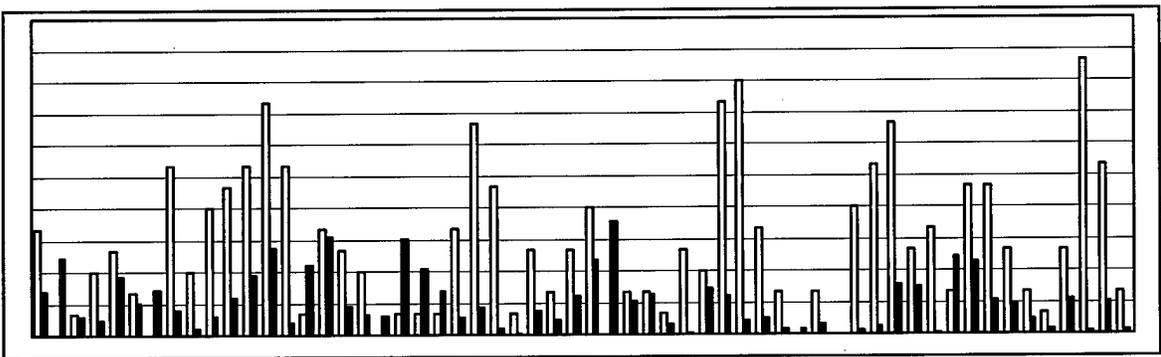
Figure 4-15. Variogram comparing Study 3 variability for a stratus case. The
light colored bars are for observed data and the dark bars are for
Simulation 3 data. The observed data exhibits a higher degree of
small-scale variability than the simulation data.

70

4.5.4 Study 4

The radiometric time series observed and simulated for study 4 were a departure from the previous studies. This study covered a 45 minute period following study 3, however, meteorological conditions had changed somewhat. The stratus cloud layers present in earlier time series gave way to stratocumulus cloud formations, with the lowest cloud layer becoming scattered and the overall vertical cloud profile consisting of three layers according to Table 4-4. Mean winds for the cloud layers were 1 m s^{-1}, 5.7 m s^{-1} and 12 m s^{-1} from the lowest to highest layers, respectively. This case study represents a midday case, so the sun's elevation angle was relatively high, peaking at 69°.

Table 4-4. Cloud Layer Information for Study 4

Layer	Cloud Type	Sky Coverage(%)	Base(m)	Top(m)
1	sc	40	400	600
2	sc	80	1500	3500
3	sc	90	7500	9000

The observed radiance time-series for this study shows that the optical depth of the cloud layers between the sun and the pyranometer decreased during the last half of the time series. This accounts for the upward trend in the data despite the fact that the sun reaches its highest point during this study and, as a result, the data should exhibit no positive trend. Complete sky coverage still exists, or radiance peaks in the time series would be an order of magnitude larger. This case study, the first of the three stratocumulus cases, shows differences in large scale variability for observed and simulation data. Here, large scale variations are taken to be peaks larger than roughly 5 $\text{W m}^{-2} \text{ sr}^{-1}$, while the small scale variations mentioned previously referred to peaks 1 W $\text{m}^{-2} \text{ sr}^{-1}$ in amplitude or less. Correlation time scales for the simulation data are shorter

71

than that of the observed data, with simulation zero-crossings generally occurring before

10 time lags, while the observed data crossed after 15 time lags as shown in Figures 4-16

(C), 4-17 (C), and 4-19 (C). The power law relationship for the simulation data was

characterized by a steeper negative slope than the observed data in all cases, consistent

with the lack of radiometric signal variation for short time scales. Likewise, variograms

showed the observed data to be more variable. Example comparisons are given in

Figures 4-18 and 4-20.
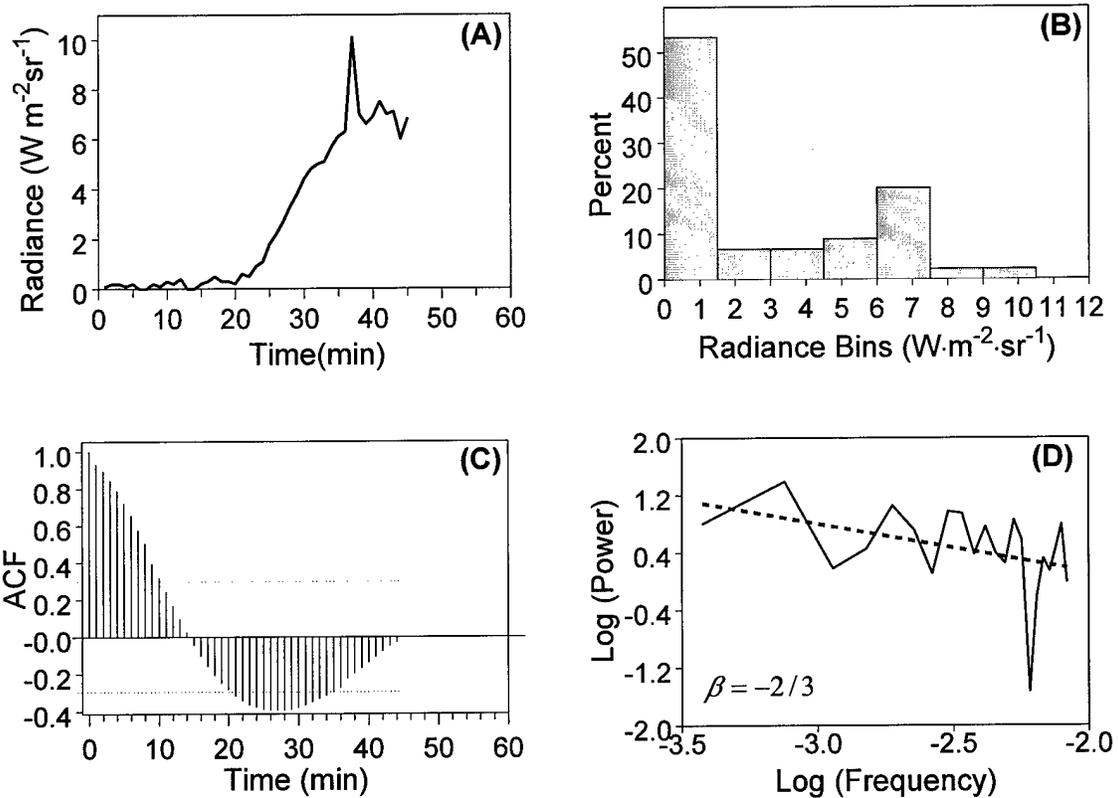
Figure 4-16. Study 4 Observed Data: (A) Radiance Time Series (B) Histogram
(C) Correlogram (D) Power Spectrum.
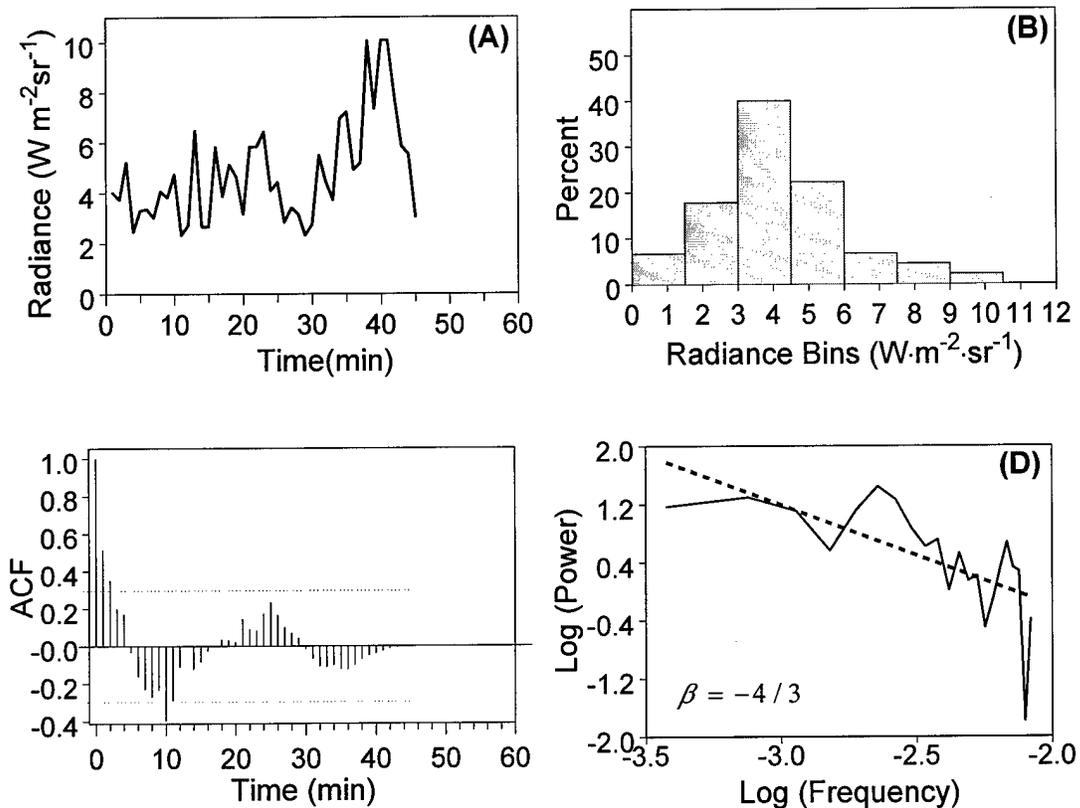
Figure 4-17. Study 4 Simulation 8 Data: (A) Radiance Time Series
(B) Histogram (C) Correlogram (D) Power Spectrum.
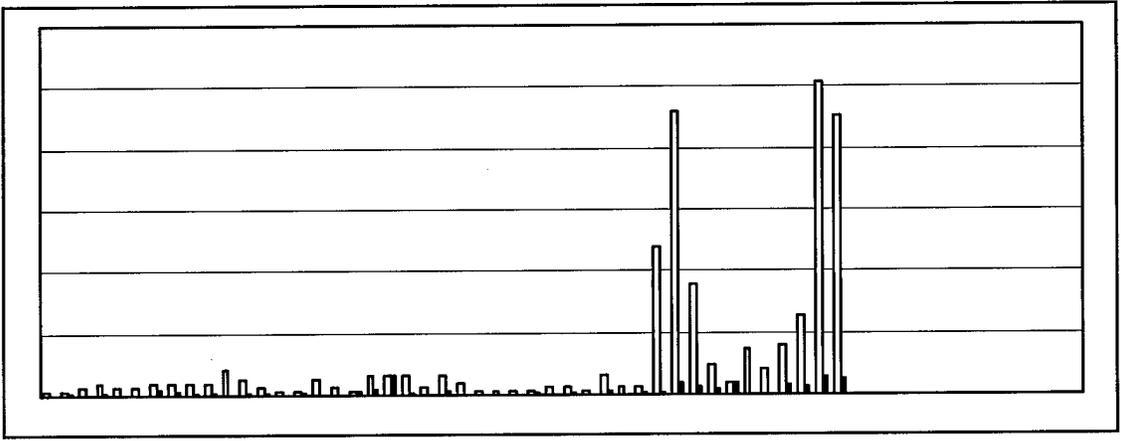
Figure 4-18. Variogram comparing Study 4 variability for a stratocumulus case.
The light colored bars are for observed data and the dark bars are
for Simulation 8 data. The observed data exhibits a higher degree
of large-scale variability than the simulation data.
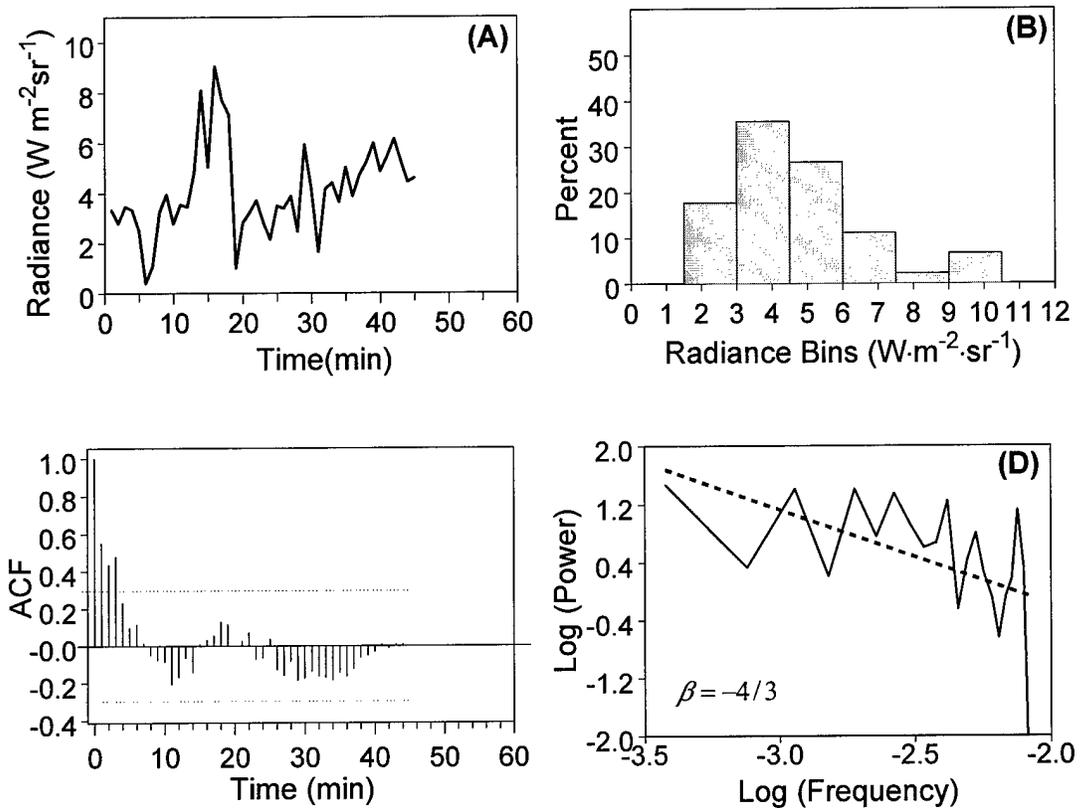
Figure 4-19. Study 4 Simulation 9 Data: (A) Radiance Time Series
(B) Histogram (C) Correlogram (D) Power Spectrum.
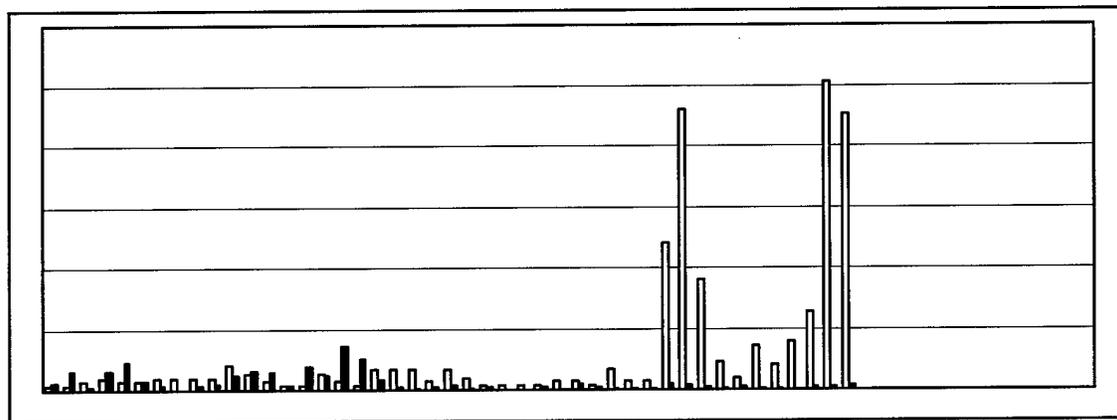
Figure 4-20. Variogram comparing Study 4 variability for a stratocumulus case.
The light colored bars are for observed data and the dark bars are
for Simulation 9 data. The observed data exhibits a higher degree
of large-scale variability than the simulation data.

74

4.5.5 Study 5

Study 5 was approximately one hour long and immediately followed study 4 in time. Stratocumulus clouds were the dominate cloud type forming in two layers vertically. Overall sky coverage decreased compared to earlier case studies for the day. This decreased coverage, together with the high elevation angle of the sun, created breaks in one or both of the cloud layers, which accounts for the large peaks in the observed and simulation time series. Table 4-5 summarizes cloud conditions present during this case study. Mean winds in the lowest layer were 4.8 m s^{-1}, and in the upper layer they were 11.8 m s^{-1}.

Table 4-5. Cloud Layer Information for Study 5

Layer	Cloud Type	Sky Coverage(%)	Base(m)	Top(m)
1	sc	70	300	4000
2	sc	75	7500	8500

The large magnitudes of the peak radiance values present in these time series made subjective analysis of small scale variations in the signal more difficult. Differences in the large scale variations were evident here. Large scale peaks were more abundant in the simulation data than the observed data. Analysis of the histogram for the observed data show 80 percent of the values collected during the time series to be less than 60 W m^{-2} sr^{-1}, and 60 percent to be less than 25 W m^{-2} sr^{-1}. The simulation data displayed more large scale variability in the signal, however, histograms in all cases were skewed to smaller values which is not surprising given the sky coverage in Table 4-5. The correlograms for this case study provided little useful information, since times to the first large-scale variation occurred near the five minute mark for all observed and

75

simulation data. The time of first zero-crossing for all cases also occurred near the five minute mark. It was interesting to note the greater number of peaks in the simulation data, which were reflected in the greater degree of periodicity in the correlogram. Power law analyses showed steeper slopes for the simulation data than for the observed data. This finding is similar to that generally found in the previous case studies, but for a different reason. In this case, the steeper slope is due to large scale variability which is greater for the simulation data. Variogram analyses for this study marked a departure from previous studies since the observed signal was dominated by large amplitude peaks. The dominate feature of the variograms in for study 5 was the large scale variability, which was greater for the simulation data. Variograms reflected this by showing that the simulation data had greater variability for most time lags in each series. Examples are provided in Figures 4-23 and 4-25.
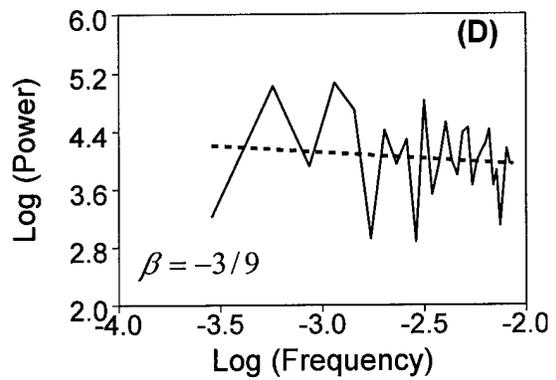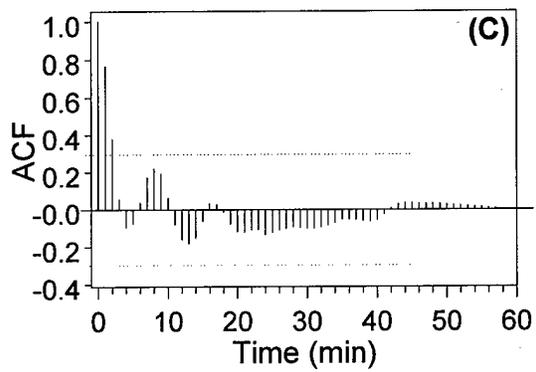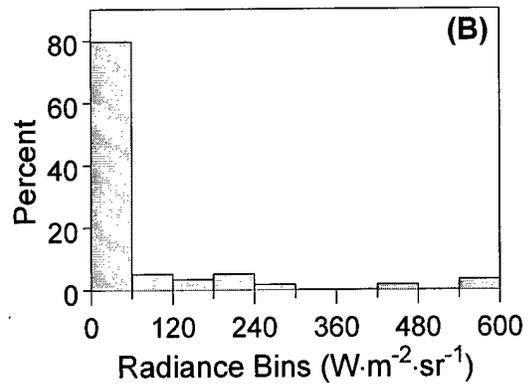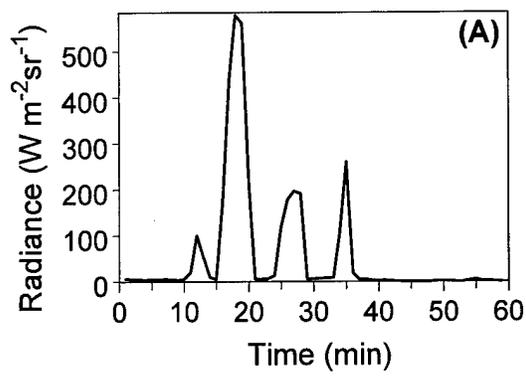
Figure 4-21. Study 5 Observed Data: (A) Radiance Time Series (B) Histogram
(C) Correlogram (D) Power Spectrum.
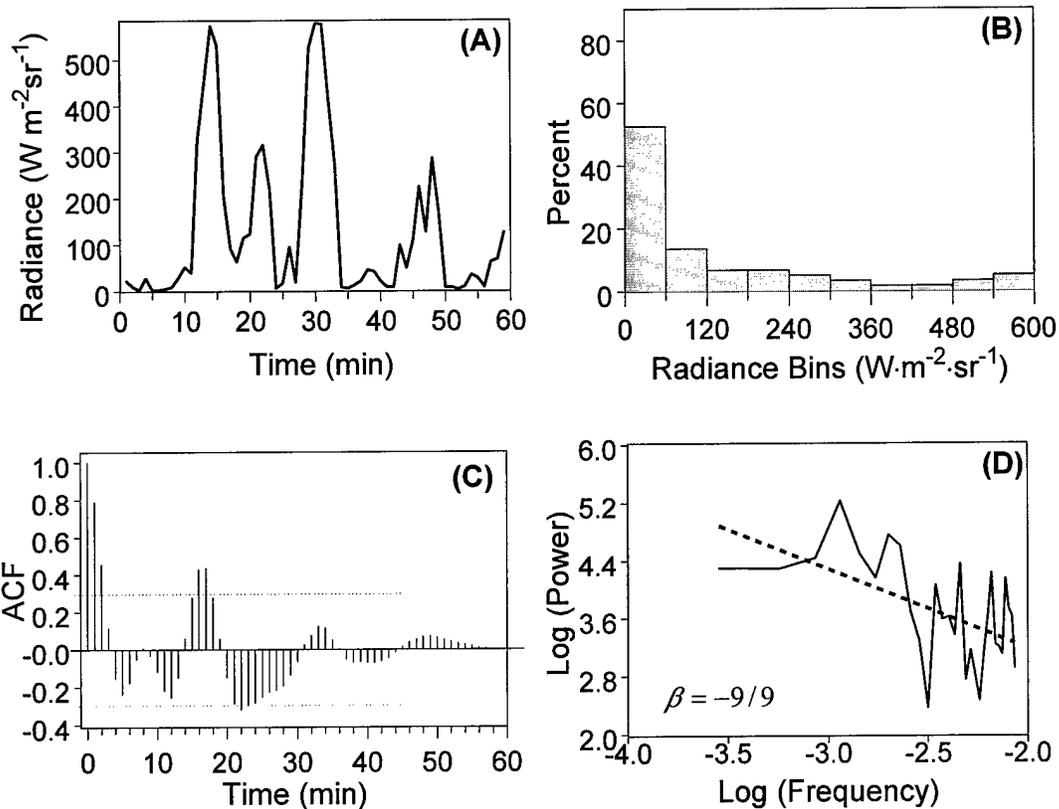
Figure 4-22. Study 5 Simulation 1 Data: (A) Radiance Time Series
(B) Histogram (C) Correlogram (D) Power Spectrum.
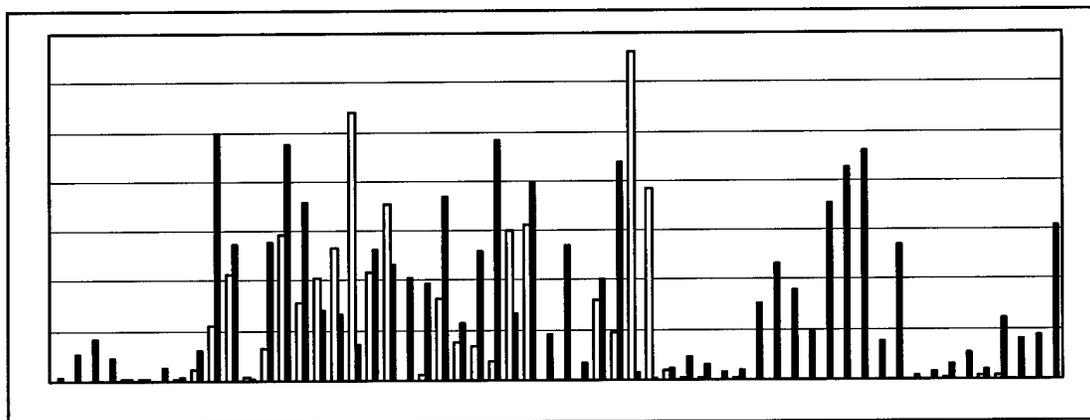
Figure 4-23. Variogram comparing Study 5 variability for a stratocumulus case.
The light colored bars are for observed data and the dark bars are
for Simulation 1 data. The observed data exhibits a higher degree
of large-scale variability than the simulation data.
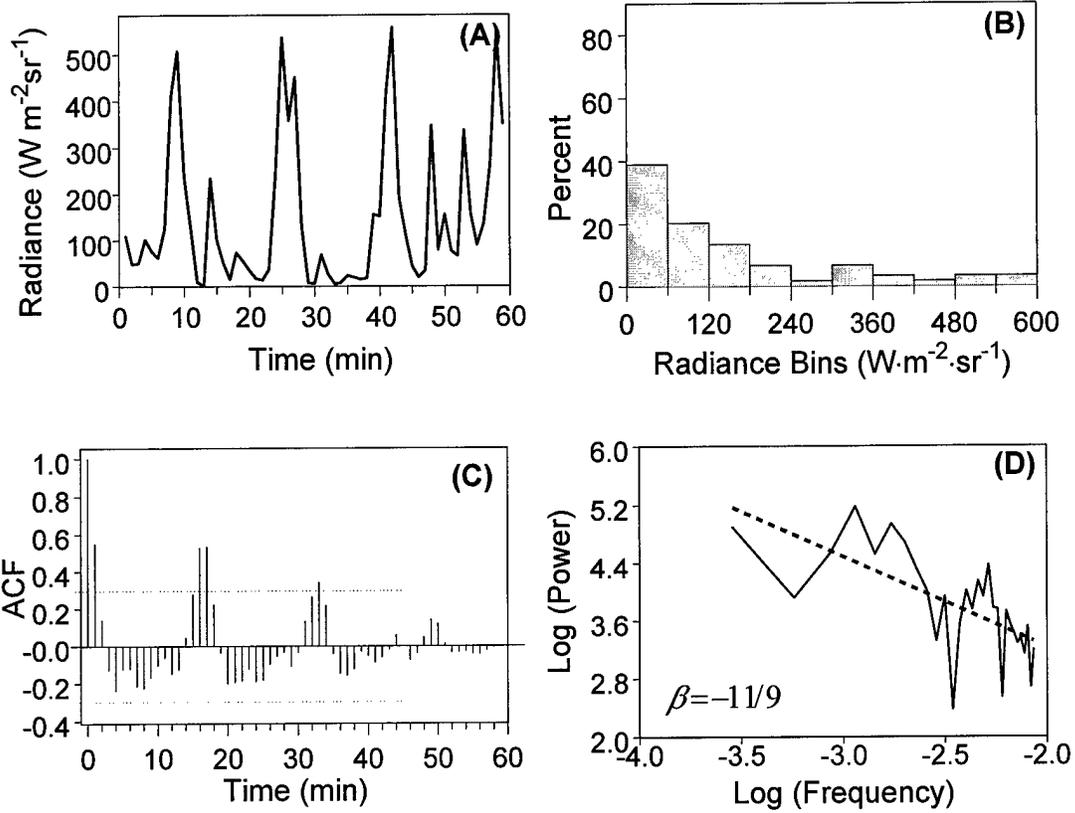
Figure 4-24. Study 5 Simulation 9 Data: (A) Radiance Time Series
(B) Histogram(C) Correlogram (D) Power Spectrum.
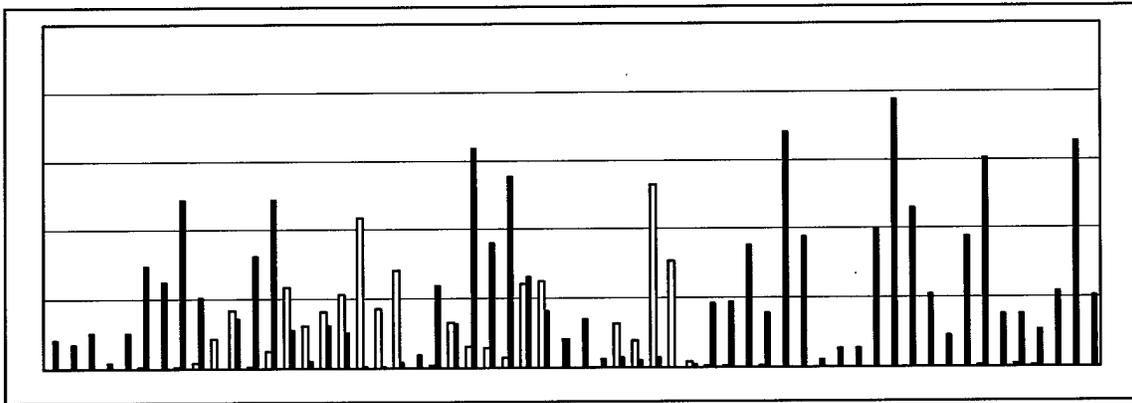
Figure 4-25. Variogram comparing Study 5 variability for a stratocumulus case.
The light colored bars are for observed data and the dark bars are
for Simulation 9 data. The observed data exhibits a higher degree
of large-scale variability than the simulation data.

4.5.6 Study 6

Study 6 spanned approximately 45 minutes immediately following study 5. The stratocumulus, two-layer system persisted, however, the percentage of sky covered by cloud decreased. Table 4-6 gives cloud layer information for Study 6. Mean winds in the lower layer were 3.9 m/s, and in the upper layer they were 11 m/s.

While the decreased cloud cover in this study created opportunities for complete breaks in the clouds, these weren't as evident as in the previous study. The lower elevation angle of the sun, from approximately $53°$ to $48°$, increased the path length through the cloud volume and reduced the overall magnitude of the peaks.

Table 4-6. Cloud Layer Information for Study 6

Layer	Cloud Type	Sky Coverage(%)	Base(m)	Top(m)
1	sc	70	200	3000
2	sc	60	7500	8000

Subjective analysis of the observed and simulation radiometric time series again show more large-scale variation in the simulation data series. Histograms are skewed toward small radiance values. However the observed data were dominated by small values to a greater extent than the simulation data. Time scale correlation lengths for the simulation time series were roughly half that of the observed data. The power law analyses were inconclusive for this study since simulation and observed slopes were nearly identical. Variograms for this case study were similar to those in study 5 in that they reflected the greater degree of large-scale variability in the simulation data.

80
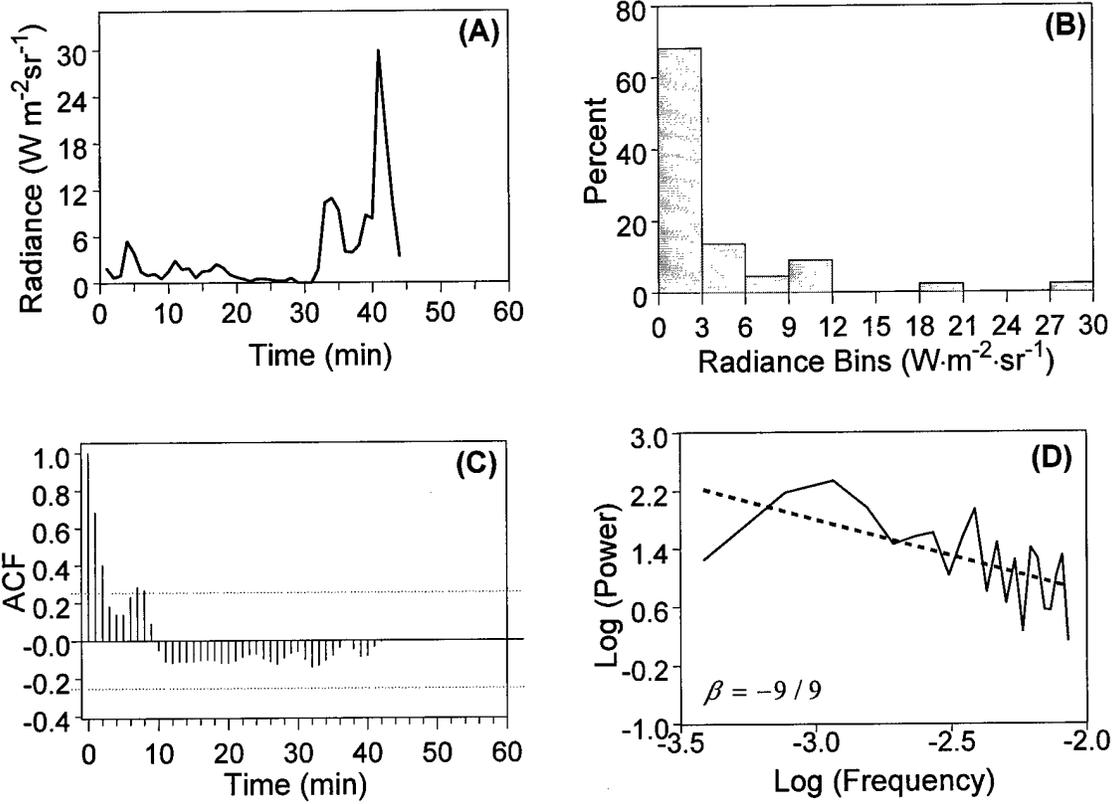
Figure 4-26. Study 6 Observed Data: (A) Radiance Time Series (B) Histogram
(C) Correlogram (D) Power Spectrum.
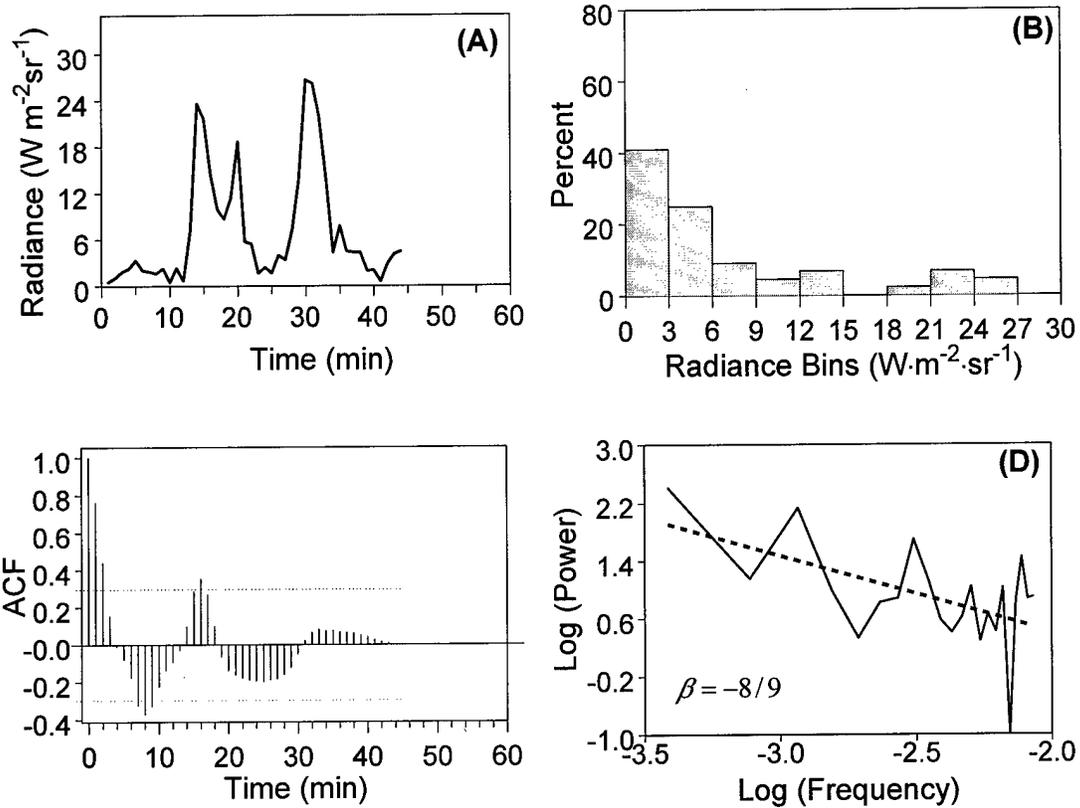
Figure 4-27. Study 6 Simulation 1 Data: (A) Radiance Time Series
(B) Histogram (C) Correlogram (D) Power Spectrum.
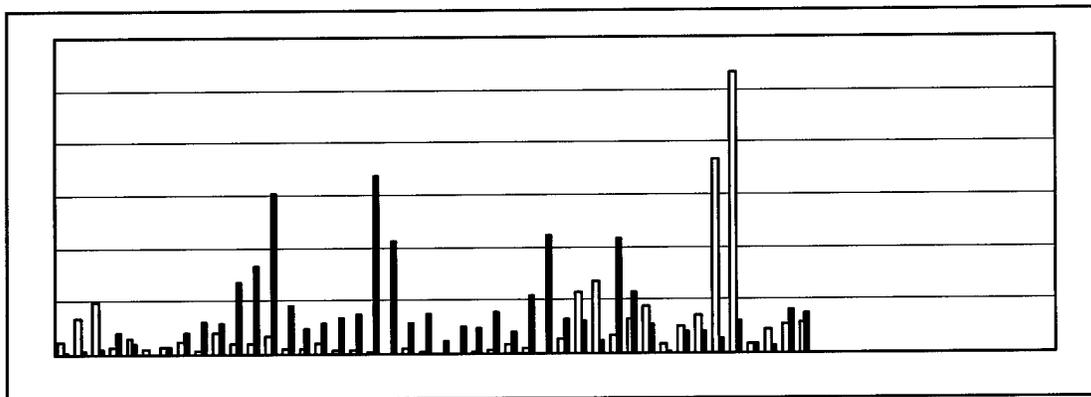
Figure 4-28. Variogram comparing Study 6 variability for a stratocumulus case.
The light colored bars are for observed data and the dark bars are
for Simulation 1 data. The observed data exhibits a higher degree
of large-scale variability than the simulation data.
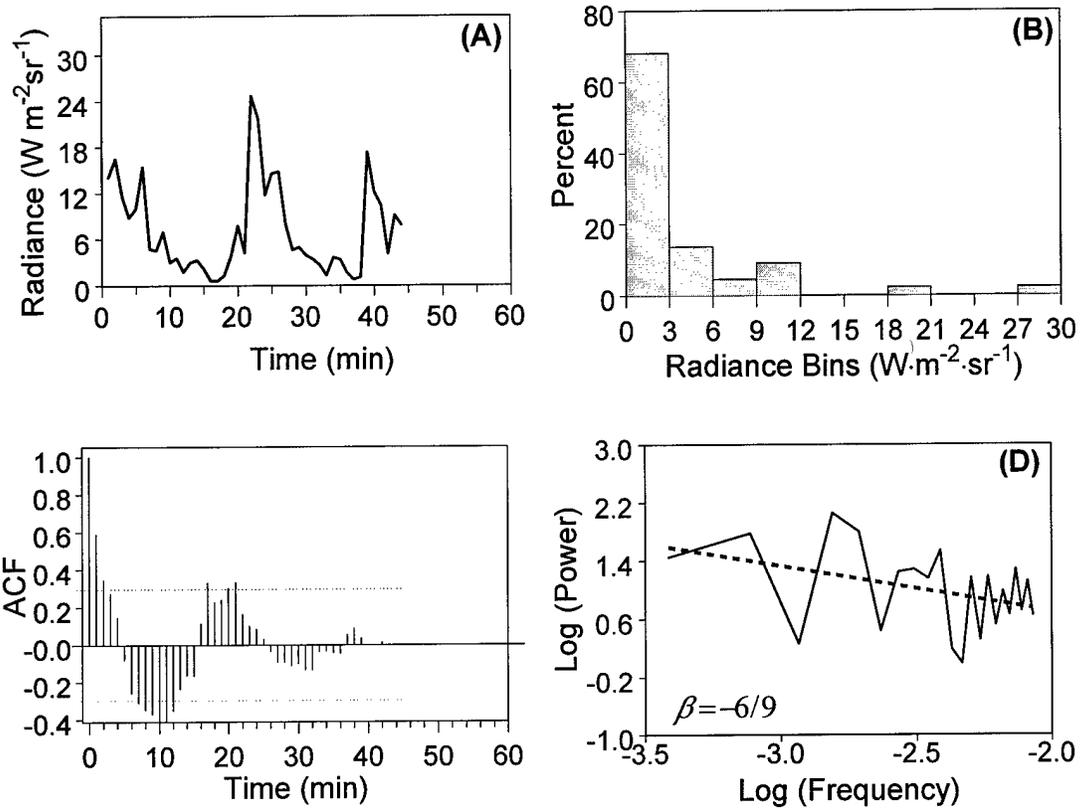
Figure 4-29. Study 6 Simulation 5 Data: (A) Radiance Time Series (B)
Histogram (C) Correlogram (D) Power Spectrum.
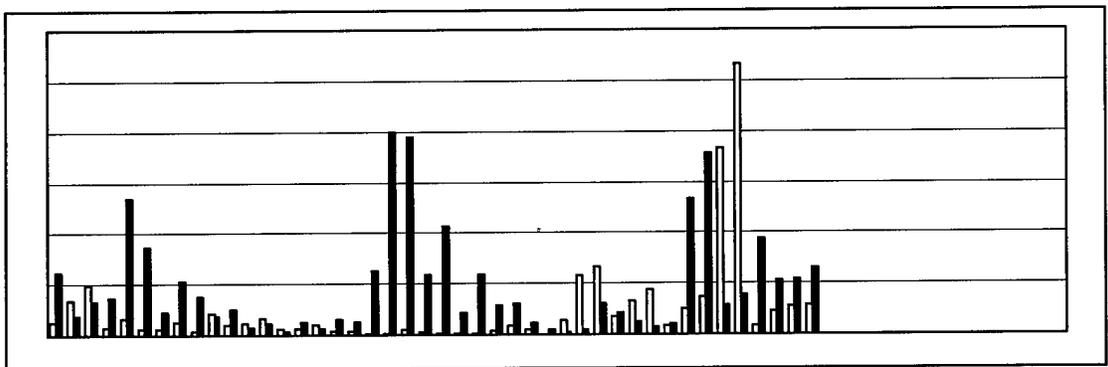
Figure 4-30. Variogram comparing Study 6 variability for a stratocumulus case.
The light colored bars are for observed data and the dark bars are
for Simulation 5 data. The observed data exhibits a higher degree
of large-scale variability than the simulation data.

5. *Conclusions and Recommendations*

This chapter presents conclusions drawn from the temporal validation study of the Cloud Scene Simulation Model (CSSM) based on the case studies presented in Chapter 4. Following these conclusions, recommendations for improving the methods employed in this validation study are made. Finally, suggestions for future research are given.

5.1 *Conclusions*

These conclusions were based on analysis of data from the 6 case studies presented in Chapter 4. Each study consisted of comparisons between an observed radiometric time series and ten simulation time series derived from CSSM model input.

The simulation radiometric time series data for stratus cloud cases did not exhibit small scale signal fluctuations present in the observed data. Small scale fluctuations are taken to be changes in signal magnitude of approximately 1 W m^{-2} sr^{-1} over a time intervals of less than 5 minutes. Histograms of radiance values indicated a wider distribution of values for stratus cases for which small scale variation was the dominate feature. Additionally, variograms showed that small scale variability of the signal was greater for the observed data in cases without large scale feature domination. Large scale feature domination manifests itself in the radiometric signal when reduced fractional sky coverage allows breaks between clouds. When large scale features did dominate, variograms showed large scale variation to be greater for most time lags in each simulation series.

Power law analyses did not provide conclusive support for this observation. This can be attributed to the small number of data points present in the time series. This type of analysis is limited by the overall time scale of the data and the Nyquist frequency, which represents the smallest time scale that can be resolved. Since all data for this validation was at 1 minute resolution, the Nyquist frequency was 2 minute^{-1}. Below this limit frequency aliasing can occur. For this reason, power amplitudes corresponding to frequencies below this limit were neglected. This reduced the number of data points used for the power law analyses to 30 points for a 60 minute time series. Many more data points are needed to accurately classify the power law relation.

The simulation time series data also exhibited more large scale variation in the radiometric signal than that of the observed data for stratocumulus cases. Large scale variations are taken to be changes in signal magnitude greater than 5 W m^{-2} sr^{-1} over time intervals greater than 5 minutes. Histograms of radiance values showed a wider spectrum of values in stratocumulus case studies for which large scale variations were the dominate feature. Correlograms indicated that correlation time scales were generally shorter for the simulation data, corresponding to a greater degree of large scale variation.

These results suggest that the CSSM does not model clouds in a realistic manner with time. Small scale variations of the radiometric signal correspond to small scale variations in the optical thickness of the intervening cloud. Given that both the real and simulated clouds are advecting with the mean wind, a difference in these variations could be attributed to a difference in the evolution of small scale cloud elements with time. The same reasoning can be used to infer a difference in the evolution of large scale features between real and simulated cloud fields.

85

5.2 Recommendations for Improving Future Validation Studies

While future CSSM temporal validation studies may make use of the methods employed in this thesis, several recommendations can be given which will improve these efforts. Primary recommendations include performing more case studies with additional data, improving the radiative transfer approach used to derive the radiometric time series and augmenting the analytical techniques used. These will now be discussed in more detail.

Many more case studies must be run to provide a sufficient amount of data from which to draw conclusions. Observed data used for these case studies should be drawn from many different days and locations as availability permits. Care must be taken while selecting this data. The validation method used in this study requires optically thick clouds with sky coverage greater than 80 percent. If these requirements are not met, it is difficult to adequately sample the cloud volume with the ray tracing routine. Also, case studies should be selected from approximately 1000 to 1400 local time. During these times the sun elevation angle is high enough to ensure that a ray traced from the position passes through the top of the simulation cloud volume.

These case studies should only be accomplished for sun elevation angles greater than $45°$, especially if the ray tracing method is retained. This reduces the chance that a ray path vector from the sun enters through the side of the cloud volume during the ray tracing portion of simulation time series production, an occurrence that must be checked for each case study. Evidence suggests that the accuracy of radiometric measurements increases with increasing elevation angle (Alberta and Cox 1990). Additionally, trends in

86

the observed data due to diurnal fluctuations in the sun's radiometric signal are smaller. This allows application of autocorrelation and power law analyses to the data without having to remove trends from the data.

Application of a full 3-dimensional radiative transfer model to calculate radiance values based on input CSSM water content grids and other parameters would be a great enhancement. Such a model would be able to account for contributions to the radiometric signal due to scattering and emission much more accurately than approximations used in this validation. It should be cautioned that such models are very expensive computationally so that the time involved in producing even a single time series may be prohibitive.

Alternatively, a Monte Carlo based radiative transfer model may be applied with more easily. While such a model would be much faster than a full 3-dimensional approach, it would still be considerably slower than the ray tracing method currently being used. A comparison of these methods would be in order to determine if the increased accuracy justified the computational expense.

5.3   Suggestions for Further Research

Ample opportunity exists for further research in this area. Incorporation of the recommendations for improving future temporal validation studies of the CSSM is the first step. The next logical step is to accomplish a sensitivity study of the temporal fractal parameters to determine their effect on temporal evolution of the cloud fields. Previous

studies have determined the effects of these parameters in the spatial dimensions

(Cianciolo and Rasmussen 1992, 1996; Turkington et al. 1998), as discussed in Chapter

2. Application of these concepts to the temporal dimension is not straightforward,

however. An iterative approach could be taken in which various combinations of

temporal RSA parameters are adjusted, new simulation time series are produced, and

comparison is made with the appropriate observed and previous simulation data sets.

Such an effort would be likely to improve the temporal performance of the CSSM in the

process, which is the major goal of this research effort.

APPENDIX A: CONVERSION OF METEOROLOGICAL DATA TO CSSM FORMAT

The format of atmospheric soundings that were provided as part of the ancillary meteorological data set was incompatible with that needed for Cloud Scene Simulation Model (CSSM) meteorological condition input files. Specifically, the soundings reported moisture in terms of relative humidity, while the CSSM required dewpoint temperature.

Since saturation vapor pressure is a function of temperature, it was possible to compute this value for the temperature at each level. This was done using a modified version of Teton's formula:

$$e_s(T) = 6.112 \cdot \exp\left(\frac{17.67 \cdot T}{T + 243.5}\right) \qquad \text{(A-1)}$$

where e_s is given in millibars, and T is the temperature in degrees Celsius. This formula is accurate to within 0.1% over -35°C ≤ T ≤ 35°C.

The saturation vapor pressure was then multiplied by the relative humidity to obtain the vapor pressure for each level. Since dewpoint temperature is the temperature at the actual vapor pressure, this value could be used to determine the dewpoint temperature according to:

$$T = \frac{243.5 \cdot \ln e_s - 440.8}{19.48 - \ln e_s} \qquad \text{(A-2)}$$

which is the inverse form of the modified Teton's formula. (Bolton 1980)

APPENDIX B: METHOD OF SCALING SIMULATED

HELIOMETER DATA

It was necessary to scale the simulated heliometer data to reproduce the dynamic range of the real heliometer data. This was done in order to make comparisons between the simulated and observed data, and, in effect, approximates solar radiation reaching the heliometer, both directly and for the case of multiple scattering.

We assume radiative transfer for a plane-parallel atmosphere, which is given by the equation:

$$I(\tau,-\mu,\varphi) = I(0,-\mu,\varphi)e^{-\tau} + \int_0^\tau J(t,-\mu,\varphi)e^{-(\tau-t)}dt \qquad \text{(B-1)}$$

where: I is the radiant energy; τ is the slant path optical depth (a unitless quantity); $-\mu$ is the solar zenith angle, with negative implying downward; ϕ is the azimuth angle; and J is the radiative source function.

If we assume isotropic scattering, then for an atmosphere in which scattering is conservative, that is, one in which there is no absorption, the source function can be written as:

$$J(\vec{r}, \vec{s}) = \frac{1}{4\pi} \int_{4\pi} P(\vec{s},'\vec{s})I(\vec{r},\vec{s})d\omega_s \qquad \text{(B-2)}$$

where: $\mathbf{r}$ is the incident radiation vector, and $\mathbf{s}$ is the scattered radiation vector. P is the scattering phase function that gives the probability of radiation being scattered into

the direction **s** from direction **s'**. This accounts for emission and scattering of radiation

into the path, and is given by:

$$J(\tau) \approx \frac{\varpi}{4\pi} I_0 P_0 e^{-\tau}$$

(B-3)

where ω is the single scattering albedo, or the ratio of scattering coefficient to total

extinction coefficient. P_0 is the probability of forward scattering. (Goody and Yung

1989)

For forward scattering along the solar ray, in the direction $-\mu$, ϕ, we can use

equation B-3 to express the radiative transfer equationB-1 as:

$$I(\tau) = I_0(0)e^{-\tau} + \int_0^\tau (\frac{\varpi \cdot I_0}{4\pi} P_0 e^{-t}) e^{-(\tau-t)} dt$$

.

(B-4)

Integrating equationB-4 gives:

$$I(\tau) = I_0(1 + c\tau) \cdot e^{-\tau}$$

(B-5)

where the constant, $c = \frac{\varpi \cdot P_0}{4\pi}$. This allows for the approximate accounting of radiation,

which has been scattered into the solar path and observed by the heliometer. It turns out

to be proportional to the slant length optical depth, τ. For the case where there is no

scattering, $P_0=0$, $c=0$, and equation B-5 reduces to the form commonly known as Beer's

Law, which only accounts for attenuation of radiation along a path.

It now remains to find a particular value for c, which will scale the simulated

radiance values to be consistent with the range of the observed data. For each time series

study, representative minimum and maximum values of radiance are selected from the observed data. These correspond to times maximum and minimum cloudiness, respectively. Finally, the largest representative optical depth value is selected from the integrated path extinction coefficients derived from each simulated cloud volume. These quantities can then be used with equation B-5 to solve for c. This constant is then used in equation B-5 along with the integrated optical depth values for each time step of each simulated time series, causing the simulated radiance values to fall within the range of the observed data. While there is some degree of approximation for the contribution of scattering to the observed normal radiance with this method, it was applied consistently to each time series, thus temporal variations were preserved (J. B. Mozer, personal communication).

BIBLIOGRAPHY

Alberta, T.L., and S.K. Cox, 1990: Cloud Field Reflectance Variations Traceable to Finite Cloud Effects, *Journal of Applied Meteorology*, **29**, pp.165-178.

Bolton, D., 1980: The Computation of Equivalent Potential Temperature, *Monthly Weather Review,* **108**, pp.1046-1053.

Burden, R.L., and J.D. Faires, 1997: *Numerical Analysis*, Brooks and Cole Publishing Company, 811pp.

Cahalen, R.F., and J.H. Joseph, 1989: Fractal Statistics of Cloud Fields, *Monthly Weather Review,* **117**, pp.261-272.

Chatfield, C., 1984: *The Analysis of Time Series – An Introduction*, J.W. Arrowsmith Ltd., 286pp.

Cianciolo, M.E., and R.G. Rasmussen, 1992: *Cloud Scene Simulation Modeling – The Enhanced Model*, Technical Report, PL-TR-92-2106, 38pp.

Cianciolo, M.E., and M.E. Raffensberger, 1996a: *Atmospheric Scene Simulation Modeling and Visualization,* Technical Report, PL-TR-96-2079, 110pp.

Cianciolo, M.E., and M.E. Raffensberger, 1996b: *Atmospheric Scene Simulation Modeling and Visualization – Cloud Scene Simulation Model User's Guide,* Technical Memorandum, TIM-7169-2, 69pp.

Davis, A., A. Marshak, et. al., 1996: Scale Invariance of Liquid Water Distributions in Marine Stratocumulus. Part I: Spectral Properties and Stationarity Issues, *Journal of the Atmospheric Sciences,* **53**, pp.1538-1558.

Eis, K.E., J.M. Forsythe, and D.L. Reinke, 1997: The Fractal Behavior of Cloud Systems, *Preprint of the Cloud Impacts on DOD Operations and Systems 1997 Conference*, PL-TR-97-2112, pp.75-78.

Feddes, R.G., 1974: A Synoptic-Scale Model for Simulationg Condensed Atmospheric Moisture, USAFETAC-TN-74-4, 56pp.

Feder, J., 1988: *Fractals*, Plenum Press, 283pp.

Goody, R.M., and Y.L. Yung, 1989: *Atmospheric Radiation – Theoretical Basis*, Oxford University Press, 519pp.

Hembree, L., et al., 1997: Incorporation of a Cloud Simulation into a Flight Mission Rehearsal System: Prototype Demonstration, *Bulletin of the American Meteorological Society*, **78**, pp.815-822.

Hentschel, H., and I. Procaccia, 1984: Relative Diffusion in Turbulent Media: The Fractal Dimension of Clouds, *Physics Review* **29**, pp.1461-1470.

Hiett, T. 1995: A User's Guide to the ACT/EOS Validation Experiment Level-2 Data Set, Technical Memorandum, Technical Report, PL-TR-95-2136, 40pp.

Lorenz, E. 1996: *The Essence of Chaos*, University of Washington Press, 240pp.

Jenkins G.M., and Watts D.G., 1968: *Spectral Analysis and its Applications*, Holden-Day, 525pp.

Lovejoy, S., 1982: Area-Perimeter Relation for Rain and Cloud Areas, *Science* **216**, pp.185-187.

Lovejoy, S., and D. Schertzer, 1985: Generalized Scale Invariance in the Atmosphere and Fractal Models of Rain, *Water Resources Research* **21**, pp. 1233-1250.

Mandelbrot, B., 1983: *The Fractal Geometry of Nature*, W.H. Freeman and Co., 468pp.

Marshak, A., A. Davis, et. al., 1997: Scale Invariance in Liquid Water Distributions in Marine Stratocumulus. Part II: Multifractal Properties and Intermittency Issues, *Journal of the Atmospheric Sciences* **54**, pp.1423-1444.

Mozer, J.B., Air Force Phillips Laboratory, Hanscom Air Force Base, Personal Correspondence.

Raffensberger, M.E., E.O. Schmidt, and M.E. Cianciolo, 1996: *Atmospheric Scene Simulation Modeling and Visualization – Fast-Map Processor User's Guide*, Technical Memorandum, TIM-7169-3, 69, 25pp.

Rys, F.S., and Waldvogel, A., 1986: Fractal Shape of Hail Clouds, *Physics Review,* **56**, pp784-787.

Saupe, D., 1989: Point Evaluation of Multi-Variable Random Fractals, *Visualisierung in Mathematik und Naturwissenschaft*, H. Jurgens and D. Saupe, Eds., Springer-Verlag, Heidelberg, pp.115-126.

Seeley, G.P., J.B. Mozer, and E. Emre, 1997: Time Series Cloud Forcing Study of Cloud Scene Simulation Model, *Preprint of the Cloud Impacts on DOD Operations and Systems 1997 Conference*, PL-TR-97-2112, pp.205-208.

Setayesh, A.A., 1996: *Integration of the PSU/NCAR Mesoscale Model (MM5) with the Phillips Laboratory Cloud Scene Simulation Model (CSSM)*, Technical Report, PL-TR-96-2098, 14pp.

Triantifiolo, S., Air Force Phillips Laboratory, Hanscom Air Force Base, Personal Correspondence.

Turkington, R.B., M.E. Cianciolo, and M.E. Raffensberger, 1998: *Development of an Atmospheric Scene Simulation Model*, Technical Report, AFRL-VS-HA-TR-98-0051, 173pp.

Wallace, J.M., and P.V. Hobbs, 1977: *Atmospheric Science – An Introductory Survey*, Academic Press Inc., 467pp.

Wilks, D.S., 1995: *Statistical Methods in the Atmospheric Sciences*, Academic Press, 467pp.

United States Naval Observatory Astronomical Applications. "Complete Sunrise and Sunset Data for One Day." http:/aa.usno.navy.mil/AA/data. 12 January 1999.

VITA

D. Glenn Kerr was born 2 December 1966 in Dallas, Texas. In May 1985, he graduated from Lansing High School in Lansing Kansas. He enlisted in the Air Force in December of that year and was stationed at Little Rock AFB as an avionics technician. While at Little Rock, he served in Operations Desert Shield and Desert Storm. He graduated from Arkansas State University in July 1991, with an Associates Degree in Mathematics. That Fall, he was accepted for the Airmans' Education and Commissioning Program and was assigned to the Florida State University (FSU) in Tallahassee, Florida to pursue a degree in meteorology. He graduated magna cum laude in May 1994 with a Bachelor of Arts degree in Meteorology. While at FSU, he was inducted into Phi Beta Kappa and The Golden Key Honor Society, as well as Chi Epsilon Pi, the meteorology honor society. Upon earning his commission, with honors, from the Air Force Officer Training School in Maxwell AFB, Alabama, he was assigned to RAF Mildenhall, England as a Wing Weather Officer. In 1997, Glenn was assigned to the Air Force Institute of Technology to earn a Master of Science degree in meteorology. Upon graduation, he will be assigned to the 88th Weather Squadron at Wright Patterson AFB, OH as a Staff Weather Officer in the modeling and simulations flight.

Glenn is married to the former Nichole Allison Williamson. They have six children, Stephanie, Jon, Seth, Ben, Ian, and Evan, ages 13, 11, 10, 7, 5, and 3, respectively.

<div align="right">

Permanent Address: 1419 W. Eisenhower Rd.
                     Lansing, Kansas 66043

</div>

REPORT DOCUMENTATION PAGE			Form Approved OMB No. 0704-0188
Public reporting burden for this collection of information is estimated to average 1 hour per response, including the time for reviewing instructions, searching existing data sources, gathering and maintaining the data needed, and completing and reviewing the collection of information. Send comments regarding this burden estimate or any other aspect of this collection of information, including suggestions for reducing this burden, to Washington Headquarters Services, Directorate for Information Operations and Reports, 1215 Jefferson Davis Highway, Suite 1204, Arlington, VA 22202-4302, and to the Office of Management and Budget, Paperwork Reduction Project (0704-0188), Washington, DC 20503.

1. AGENCY USE ONLY *(Leave blank)*

2. REPORT DATE
March 1999

3. REPORT TYPE AND DATES COVERED
Final

4. TITLE AND SUBTITLE
A Validation Study of Cloud Scene Simulation Model Temporal Performance

5. FUNDING NUMBERS

6. AUTHOR(S)
D. Glenn Kerr, Capt USAF

7. PERFORMING ORGANIZATION NAME(S) AND ADDRESS(ES)
AFIT/ENP
2950 P. Street
Wright-Patterson AFB, OH 45433
Attn: LtCol Michael K. Walters   COMM: (937) 255-3636   DSN: 785-3636
        mwalters@afit.af.mil

8. PERFORMING ORGANIZATION REPORT NUMBER

AFIT/ENP/99M-08

9. SPONSORING/MONITORING AGENCY NAME(S) AND ADDRESS(ES)
88 WS/WEA
2049 Monahan Way, Bldg. 91, Area B
Wright-Patterson AFB, OH 45433
Attn: LtCol John M. Lanicci   COMM: (937) 255-2207   DSN: 785-2207
        JOHN.LANICCI@88abw.wpafb.af.mil

10. SPONSORING/MONITORING AGENCY REPORT NUMBER

11. SUPPLEMENTARY NOTES

12a. DISTRIBUTION AVAILABILITY STATEMENT
Approved for public release; distribution unlimited

12b. DISTRIBUTION CODE

A

13. ABSTRACT *(Maximum 200 words)*

Cloud Scene Simulation Model (CSSM) temporal performance was validated by comparing the cloud forcing signatures on observed radiometric time series with those derived from CSSM output for initial conditions similar to that for the observed data. Observed radiometric data was collected by a normal incidence pyraheliometer sensitive to wavelengths in the range .3mm to 3mm. Simulation radiometric time series data was derived by applying the following process to each case study. CSSM cloud liquid water content (CLWC) grids were converted to grids of slant path optical depth values by the Fast Map post processor to the CSSM. A ray tracing routine then integrated the slant path optical depth values along a path from the position of the sun through each cloud volume to a point at its base. The position of the sun was fixed by ephemeris calculations for the time and location of the case study. The integrated optical depth values were then used with a modified form of Beer's Law to derive radiometric time series values.

Subjective and statistical comparison of the observed and corresponding simulation time series data were then made. The statistical comparison used correlograms, variograms and power law analyses to determine whether CSSM cloud field evolution with time proceeded in a realistic manner.

Results indicate that CSSM cloud fields do not evolve in a realistic manner. Radiometric traces derived from simulation data lack small scale variations present in the observed data, while large scale variations in the simulation data are exaggerated.

14. SUBJECT TERMS
cloud, simulation, fractal, CSSM, temporal, validation, radiometric, time-series

15. NUMBER OF PAGES
110

16. PRICE CODE

17. SECURITY CLASSIFICATION OF REPORT	18. SECURITY CLASSIFICATION OF THIS PAGE	19. SECURITY CLASSIFICATION OF ABSTRACT	20. LIMITATION OF ABSTRACT
Unclassified	Unclassified	Unclassified	UL